



Dynamics of dissolved inorganic carbon in the South China Sea: A modeling study

Chuanjun Du^{a,b}, Jianping Gan^b, Chiwing Rex Hui^b, Zhongming Lu^b, Xiaozheng Zhao^b, Elliott Roberts^a, Minhan Dai^{a,*}

^a State Key Laboratory of Marine Environmental Science, College of Ocean and Earth Sciences, Xiamen University, Xiamen, China

^b Department of Ocean Science and Department of Mathematics, Hong Kong University of Science and Technology, Hong Kong, China

ARTICLE INFO

Keywords:

South China Sea
Dissolved inorganic carbon
Coupled physical-biogeochemical model
Budget and fluxes

ABSTRACT

Using a validated, three-dimensional, coupled physical-biogeochemical model, this study examines the dynamics of dissolved inorganic carbon (DIC) in the South China Sea (SCS). The model identifies characteristic differences in DIC concentrations between the SCS and adjacent West Philippine Sea (WPS), showing an increase in DIC of up to $140 \mu\text{mol kg}^{-1}$ in the upper 2000 m layer from the WPS to the vicinity of the northern SCS. This increasing pattern continues from the northern to the southern SCS, but to a much lower degree ($< 20 \mu\text{mol kg}^{-1}$ increase). Overall, spatial and seasonal variation of DIC in the SCS are evidently modulated by both intrinsic dynamics (e.g., river plumes, vertical mixing, basin-scale upwelling and eddies), and extrinsic exchanges via various straits. The inputs of DIC to the SCS are mainly through the Luzon Strait in the upper layer (depth, $h < 600$ m) and from the deep WPS at > 1600 m. Exports of DIC occur through other straits and the SCS intermediate water outflow (600 m to 1600 m) via the Luzon Strait. The model shows upward transport of DIC in the upper 400 m and below 1100 m, in contrast to downward DIC transport between 400 m and 1100 m. Seasonally, both DIC concentrations and fluxes in the upper layer have larger dynamic ranges in winter than in summer, attributable to the combined effects of enhanced Kuroshio intrusion, stronger vertical upwelling and greater biogeochemical alterations.

A balance of various constitutive DIC terms revealed that horizontal and vertical advection is an order of magnitude greater than the other terms of the DIC budget, which has an opposite sign and thus tends to neutralize each other. The model indicated a decrease in the DIC inventory in the euphotic zone in spring and summer caused by net DIC consumption, and a contrasting increase in fall and winter primarily influenced by DIC vertical transport. In intermediate and deep layers, physical transport processes play a dominant role in the seasonal variation of DIC inventories. In the upper 150 m, DIC fluxes and their stoichiometry with nutrient fluxes, which potentially impact the air-sea CO_2 fluxes, are largely driven by excess vertical DIC fluxes compared to horizontal fluxes via the Luzon Strait.

1. Introduction

Ocean margins play a disproportionately important role on air-sea CO_2 fluxes and the global carbon budget (Dai et al., 2013 and references therein). Global ocean margins act as a sink of atmospheric CO_2 but flux estimates range, from 0.15 to 0.4 Pg C yr^{-1} , primarily due to under-sampling (e.g., Borges et al., 2005; Cai, 2011; Cai et al., 2006; Cao et al., 2020; Chen and Borges, 2009; Dai et al., 2013; Laruelle et al., 2018). Mechanistic understanding required to address questions on why some ocean margins act as a CO_2 source while others act as a CO_2 sink with respect to the atmosphere remains insufficient. This is primarily due to

the fact that carbon dynamics in ocean margins are associated with large spatiotemporal variation in carbon fluxes that are modulated by a combination of complex physical and biogeochemical processes. Moreover, ocean margins are located transitionally between the land and open ocean, and are thus extrinsically modulated by both riverine inputs and exchange with the open ocean (Dai et al., 2013). They are thus characterized by higher spatiotemporal gradients of almost all chemical and biotic parameters. The above factors increase the difficulties of undertaking biogeochemical studies in ocean margins.

This complexity of coupled physical-biogeochemical processes along ocean margins makes the implementation and parameterization

* Corresponding author.

E-mail address: mdai@xmu.edu.cn (M. Dai).

<https://doi.org/10.1016/j.pocean.2020.102367>

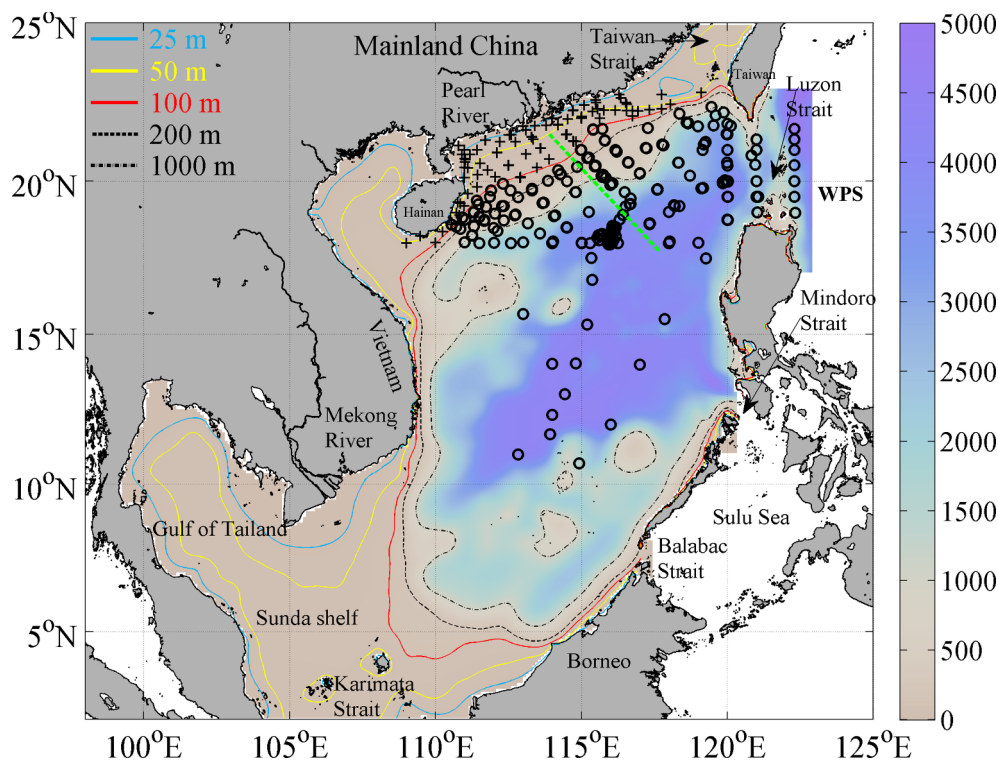


Fig. 1. Map of the South China Sea showing bathymetry, i.e., isobaths at 25 m, 50 m, 100 m, 200 m and 1000 m indicated by contour lines. A green dotted line extending from the Pearl River estuary to the northern basin denotes Section A which has been a frequent site of observations by the Chinese scientific community (see text). The observational stations used for model validation are indicated by black crosses (shelf) or circles (basin).

of numerical models a daunting challenge. The difficulty in modeling ocean margin biogeochemistry is also associated with the need to account for multiple scale domains, as boundary conditions include global, regional and estuarine scales. A further modeling challenge involves the lack of suitable initial conditions with adequate spatio-temporal resolution given that these greatly impact model performance (Hofmann et al., 2011).

The South China Sea (SCS, Fig. 1), the largest marginal sea of the North Pacific, is a complex ocean margin system with dynamic water exchange with the West Philippine Sea (WPS) via the Luzon Strait, the East China Sea via the Taiwan Strait, the Java Sea via the Karimata Strait, and the Sulu Sea via the Mindoro and Balabac Strait. Among these, the Luzon Strait is particularly wide and deep (>2000 m), and plays a key role in circulation and material transport within the SCS and the exchange with adjacent regions. Prior studies revealed a ‘sandwich’ transport structure across the Luzon Strait with influx at the upper and deep layers and outflux at the intermediate layer (Chen et al., 2001; Gan et al., 2016a, 2016b; Qu et al., 2000; Tian et al., 2006; Yang et al., 2011). Recently, Gan et al. (2016a, 2016b) further described a three-layer, cyclonic–anticyclonic–cyclonic (CAC) circulation structure in the SCS that is constrained by both extrinsic and intrinsic dynamics.

Due to inter-basin and/or inter-shelf differences in dissolved inorganic carbon (DIC) concentrations, water transport/exchanges greatly impact DIC characteristics and dynamics in the SCS. Moreover, the SCS is characterized by abundant riverine inputs from the surrounding land, which could also impact the carbonate system in the SCS (Cao et al., 2011b). The SCS is known to be a unique regime with intensive turbulent mixing (Tian et al., 2009), upwelling (Gong et al., 1992), and a permanently stratified basin.

Over the past two decades a number of studies, primarily based on field observations, have been conducted to resolve carbonate dynamics in the SCS (e.g., Cao et al., 2011, 2020, Chou et al., 2005, 2006, 2007a, 2007b; Dai et al., 2013; Sheu et al., 2009, 2010; Tseng et al., 2007; Zhai et al., 2013). They showed that the SCS acts as an atmospheric source of CO₂ (Chai et al., 2009; Li et al., 2020; Sheu et al., 2010; Zhai et al., 2005, 2013). The SCS basin has been categorized as an Ocean-dominated Margin (OceMar), where dynamic interactions with the open

ocean could provide non-local CO₂ sources, thereby modulating the CO₂ fluxes therein (Cao et al., 2020; Dai et al., 2013). However, there are several fundamental questions about DIC dynamics in the SCS that warrant further consideration. Due to the limitations of field observations, understanding of the spatiotemporal variation of DIC and its controlling mechanisms remain to be fully described. Transport/exchange of DIC with adjacent seas and within the SCS also need to be further examined, particularly in light of new understanding on water fluxes. Finally, the impacts of vertical and horizontal DIC exchanges, and the stoichiometry of DIC relative to nutrients on the carbon cycle are unclear. Thus, the relative contributions to the DIC budget of both physical and biogeochemical processes need to be elucidated.

This study examines the spatial distribution and seasonal variation of DIC in the SCS using a three-dimensional, coupled physical-biogeochemical model. The impacts of physical and biogeochemical processes on the DIC budget are assessed and DIC dynamics is further discussed in relation to extrinsic and intrinsic exchange fluxes.

2. Methods

2.1. Physical-biogeochemical model

Analyses in this study are based on a three-dimensional coupled physical-biogeochemical model based on the China Sea Multiscale Modeling System (CMOMS, Gan et al., 2016a, 2016b). It is a Regional Ocean Modeling System (ROMS) established in the northern Pacific, extending from ~0.95°N, 99°E to the southeast corner of the Sea of Japan (Gan et al., 2016a, 2016b). The horizontal resolution of the model increases from ~10 km in the southernmost region to ~7 km in the north. The model has 30 levels in the vertical direction, which is forced by wind stress, and atmospheric fluxes (climatological forcing), and external fluxes from a global model, i.e., tides and active, open boundary conditions (OBCs) (Gan et al., 2016b). By considering the linked physics associated with the western boundary current, monsoon winds, tidal forcing, and topography in the marginal seas west of the Pacific Ocean, the model successfully captures the observed physical properties and water transport in the marginal seas, including the SCS.

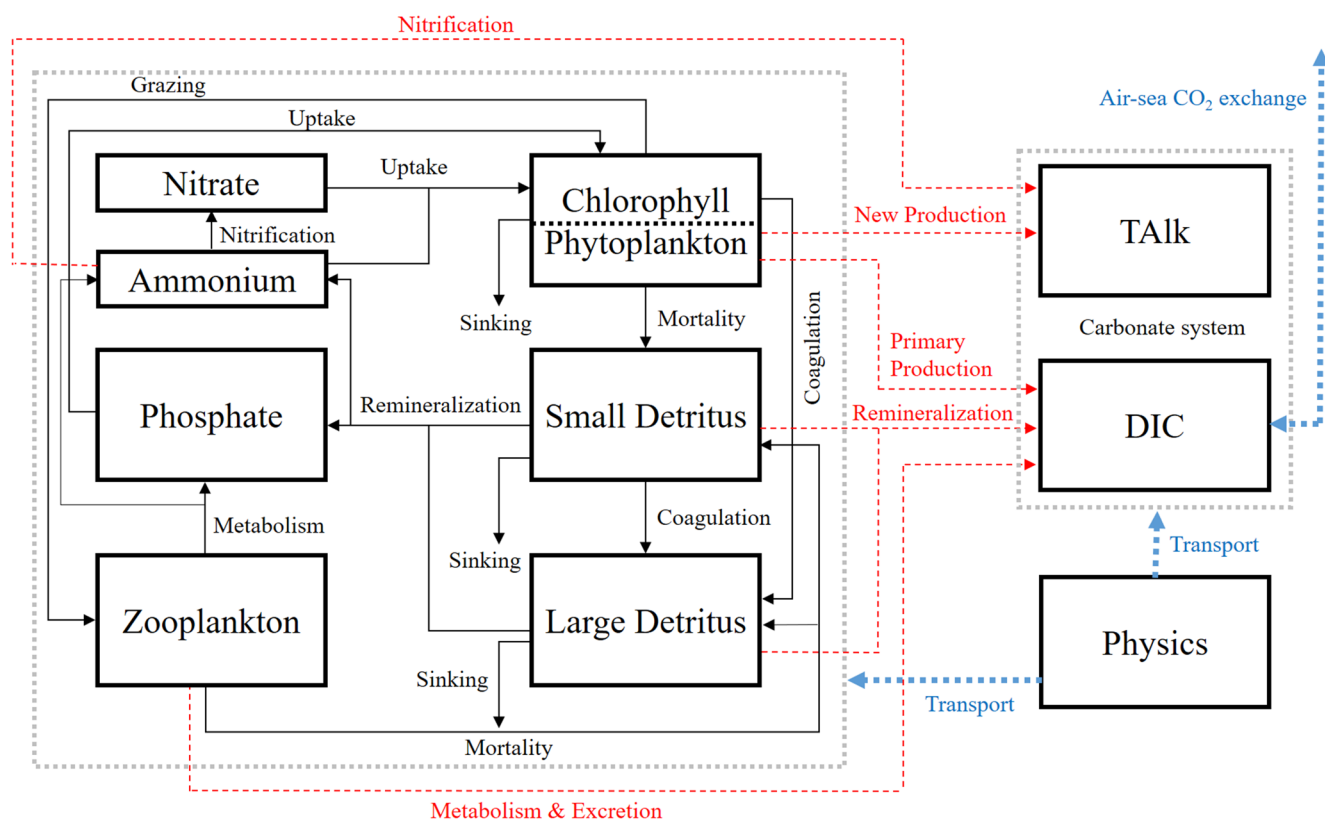


Fig. 2. Schematic diagram of the biological, nutrient, and carbonate system modules in the China Sea Multiscale Modeling System (CMOMS) adopted from Gan et al. (2014) and Lu et al. (2012, 2020). Biogeochemical processes relating to dissolved inorganic carbon (DIC) and total alkalinity (TALK) are plotted using red and blue arrows.

Implementation details of the physical model and validation of the dynamics and hydrography are presented in Gan et al. (2016a, 2016b).

The biogeochemical component of the model uses a Nitrogen-Phytoplankton-Phosphorus-Zooplankton-Detritus (NPPZD) module (Gan et al., 2014; Lu et al., 2020), which includes nitrate (NO_3^-), ammonium (NH_4^+), dissolved inorganic phosphate (DIP), phytoplankton, zooplankton, and two detrital size fractions i.e. a small and large detritus (Fig. 2). It is upgraded from a prior NPZD module by including DIP limitation to better simulate nutrient assimilation, particularly in plume areas (Gan et al., 2010; Lu et al., 2012; Fennel et al., 2006). The carbonate system module is connected to the nitrogen module via a C:N ratio of 6.625 (Lu et al., 2012). In addition to physical transport, DIC is modulated by phytoplankton carbon primary production, detritus remineralization, zooplankton metabolism and excretion rates, and CO_2 air-sea exchange (Fig. 2). The CO_2 air-sea fluxes are calculated according to Wanninkhof (1992) and Weiss (1974). The total alkalinity (TALK) is modulated by NO_3^- uptake and nitrification. The equations and parameterization of the biogeochemical modules are presented by Gan et al. (2010, 2014), and Lu et al. (2012).

The model is initialized with temperature, salinity, NO_3^- and DIP obtained from the winter World Ocean Atlas 2013 (WOA2013; <https://www.nodc.noaa.gov/>); OBCs and initializations for DIC and TALK are obtained from interpolation of the GLObal Ocean Data Analysis Project (GLODAP) dataset (<http://cdiac.ornl.gov/oceans/glodap/>). Since the GLODAP data domain does not include the SCS, the winter GLODAP data in the adjacent WPS were used in conjunction with winter observations (see Section 2.2) to obtain the initial DIC and TALK in the SCS. The initial and boundary conditions of temperature, salinity, NO_3^- and DIP, DIC and TALK in the dataset grid are interpolated to fit the model grid and smoothed. Active OBCs (Liu and Gan, 2016) was used for all variables to resolve tidal or subtidal flows along the open boundaries of the model domain.

As the NO_3^- and DIP initial conditions from the WOA are ill-suited for the SCS, the model was run for 50 years to reach a quasi-steady state and reduce the residual effect of the initial conditions (Fig. S1). The weekly mean variables in the last five years are used for the analyses.

2.2. Observational data

Data collected from field observations, covering four cruises and a seasonal cycle during 2009–2011 in the northern SCS (nSCS) is used to validate the model. The details of cruises, sampling, and measurement of nutrient and carbonate samples were presented in previous studies (Cao et al., 2011a; Dai et al., 2013; Du et al., 2013; Du et al., 2017; Guo et al., 2015), including data in Roberts et al. (2020) and/or in preparation. Observations in the middle and southern SCS (sSCS) basins (Fig. 1; $< 17^\circ\text{N}$) were obtained from the Taiwan KEEP project (ORI-508 and ORI-546 cruises; <https://www.nodc.noaa.gov/>). Details of the cruises, sampling, measurements and data were published by Chen et al. (2006).

3. Results

3.1. Model validation

Since the physical model largely follows the CMOMS model (Gan et al., 2016a, b), this study mainly focuses on the biogeochemical model components. To assess model performance, the model is validated by comparing model results point-by-point with the observations through iso-surface, sectional and vertical distributions (Figs. 3–6 and S3–S4). To allow better comparisons, model data were interpolated to match the resolution of observations. As the model is forced by climatological wind and boundary conditions, an inter-annual difference exists between these comparisons. March to May are defined as spring, June to

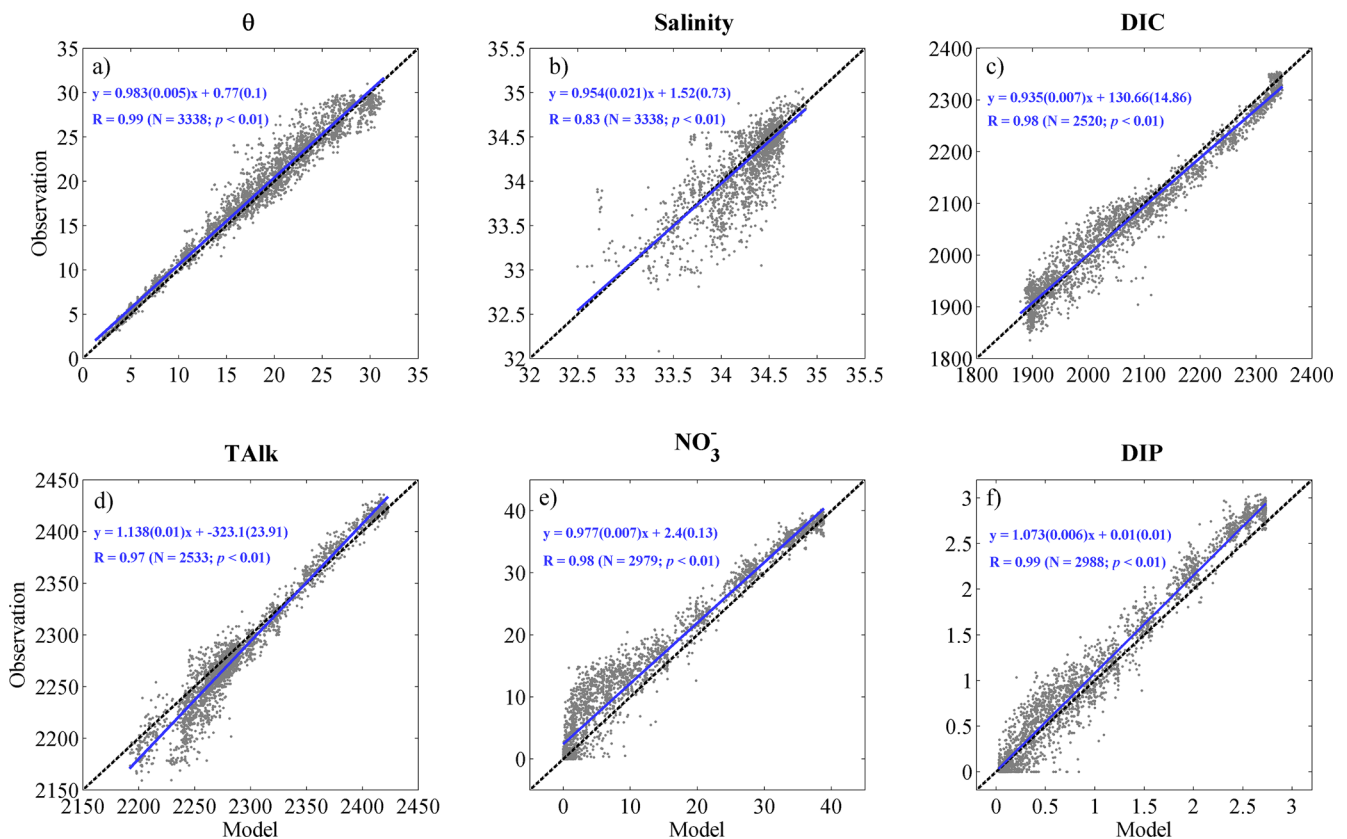


Fig. 3. Model simulations versus observations: (a) potential temperature (θ , °C); (b) salinity; (c) dissolved inorganic carbon (DIC, $\mu\text{mol kg}^{-1}$); (d) total alkalinity (TAlk, $\mu\text{mol kg}^{-1}$); (e) NO_3^- ($\mu\text{mol L}^{-1}$); and (f) dissolved inorganic phosphate (DIP, $\mu\text{mol L}^{-1}$) in the basin area (depth > 100 m). The black dashed line is the 1:1 line. The blue line is the fitted regression line; the regression equation and its associated standard deviations of the slope and intercept, correlation coefficient (R) and significance, p value, are also shown.

August as summer, September to November as fall, and December to February as winter in the SCS.

The point-by-point comparisons of potential temperature (θ), salinity, DIC, TAlk, NO_3^- and DIP between model simulations and observations in the basin are shown in Fig. 3. The correlation between observed θ and simulated data is significant with a correlation coefficient (R) of 0.99 ($p < 0.001$). The slope of the linear regression is 0.983 ± 0.005 standard deviation, i.e., close to the 1:1 line (Fig. 3a). The simulated salinity does not compare quite as well with observations. Although the slope of the linear regression is 0.954 ± 0.021 , close to the 1:1 line (Fig. 3b), R equals 0.83 ($p < 0.001$) and there are significant discrepancies in the lower range of salinities, mostly in surface water. These are likely related to the uncertainty in the forcing field of the precipitation-evaporation data, generated by the bias associated with the climatological, monthly averaged meteorological variables in the Reanalysis 1 product provided by the National Centers for Environmental Prediction (NCEP).

The observed and simulated DIC values generally follow the 1:1 line and the linear slope is 0.935 ± 0.007 with a correlation coefficient R of 0.98 ($p < 0.001$) (Fig. 3c), indicating that the model generally performs well. The model overestimates of $17.0 \pm 17.0 \mu\text{mol kg}^{-1}$ at DIC concentrations > $2100 \mu\text{mol kg}^{-1}$, a result likely due to the overestimate of DIC concentrations in the adjacent WPS (Fig. S2). Simulated and observed TAlk values also generally follow the 1:1 line (Fig. 3d). The model slightly overestimates (by $\sim 0.5\%$) TAlk, equal to $11.0 \pm 16.0 \mu\text{mol kg}^{-1}$ at TAlk values < $2300 \mu\text{mol kg}^{-1}$. Optimization of TAlk simulations is an ongoing effort; thus, this study focuses on DIC dynamics.

The slope of the linear regression between observed and simulated NO_3^- values is 0.977 ± 0.007 with R equals to 0.98 ($p < 0.001$)

(Fig. 3e). The model underestimates NO_3^- by $2.4 \mu\text{mol L}^{-1}$ throughout the water column. Similarly, DIP comparisons yield a slope of 1.073 ± 0.010 with R equals to 0.99 ($p < 0.001$) (Fig. 3f). The model underestimates DIP by $< 0.20 \mu\text{mol L}^{-1}$, primarily in deep layers.

Comparisons of simulated-observed θ , DIC, TAlk and NO_3^- values in surface water of the nSCS are shown in Fig. 4. In summer, surface θ in the basin is generally higher than that on the shelf, particularly that in coastal waters (Fig. 4a, b). In contrast, θ in winter is clearly lower in the entire nSCS (Fig. 4i, j). The θ difference between the shelf and basin still exists, but the difference in magnitude increases. The model exhibits similar distribution patterns to the observations. In summer, DIC concentrations in the basin are mostly higher than on the shelf (Fig. 4c, d), except for the northeast coast where they are higher than in adjacent waters. This pattern is consistent with previous studies, which showed that the combined effect of river plumes and coastal upwelling control the DIC distribution (Cao et al., 2011b). In winter, DIC concentrations are mostly higher than in the summer both in the basin and on the northern shelf (Fig. 4k, l). Compared to the basin, DIC concentrations are evidently higher on the northern shelf. The model is able to simulate the higher DIC values in the nSCS; however, it underestimates the magnitude of the increase in DIC concentrations on the northern shelf. One likely explanation may be that the model underestimates DIC concentrations in the China Coastal Current in winter, which transports water with higher DIC concentrations from the East China Sea to the northern SCS and increases DIC values therein (Chou et al., 2011). The spatial distribution and seasonal variation of TAlk generally resemble those of DIC (Fig. 4e, f, m, n), except for the higher TAlk values found in the middle sector of the nSCS shelf in winter (Fig. 4m, n). Nitrate concentrations both in summer and winter are higher in coastal zones, then decrease moving offshore onto the shelf, and are lowest in the

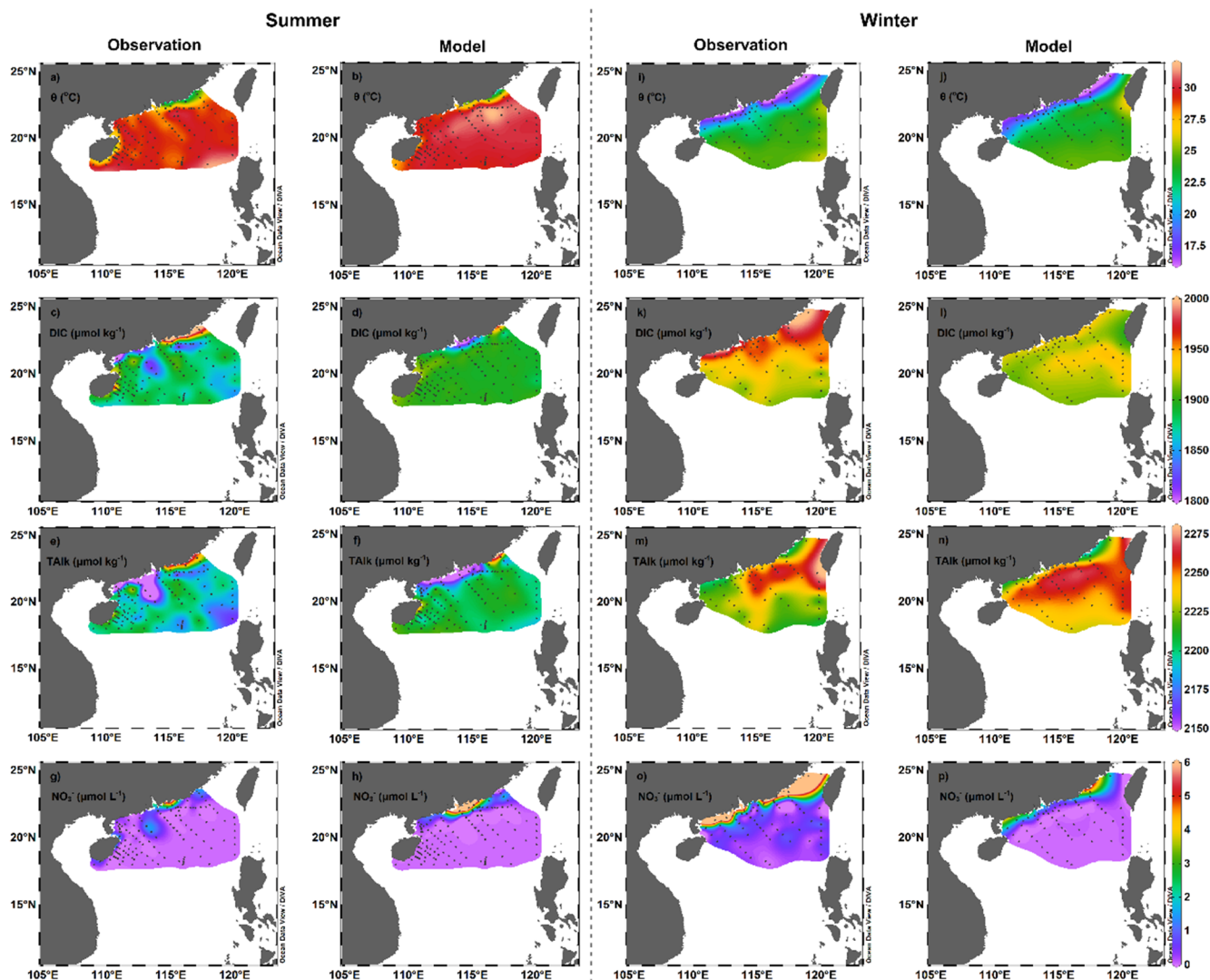


Fig. 4. Spatial distributions of potential temperature (θ), dissolved inorganic carbon (DIC), total alkalinity (TAlk), and nitrate (NO_3^-) in surface water. The eight left- and right-hand panels denote comparisons in summer, and winter, respectively. Model results are plotted to the right of the observations.

basin (Fig. 4g, h, o, p). The model generally shows similar patterns to those of the observations.

Fig. 5 compares simulated and observed DIC and NO_3^- distributions at Section A, extending from the Pearl River estuary (PRE) to the northern basin (indicated by the green dashed line in Fig. 1). It shows that both DIC and NO_3^- concentrations increase with increasing depth. At the same depth, the basin generally shows higher DIC and NO_3^- concentrations than those found on the shelf (Fig. 5). The model shows a similar pattern to these observations.

Profiles of θ , salinity, DIC and NO_3^- in the SCS basin (Sta. South East Asian Time-series Study (SEATS) (116°E, 18°N) and the WPS (122°E, 20–20.5°N) are shown in Fig. 6. The θ in the SCS basin is much lower than that in the WPS in the upper 800 m, but this pattern is reversed at depths > 800 m (Fig. 6a). In addition to an observed salinity maximum at ~ 150 m and a salinity minimum at ~ 600 m (Fig. 6b), salinity in the SCS is evidently lower than that in the WPS in the upper 400 m and at depths > 1800 m, but shows a reversal in this relationship at depths (h) $400 < h < 1800$ m. Concentrations of DIC in the SCS are evidently higher than those in the WPS by up to $140 \mu\text{mol kg}^{-1}$, especially between 100 and 600 m (Fig. 6c). The NO_3^- concentrations in the SCS are higher than those in the WPS at depths > 800 m and < 2300 m, but show an inverse pattern at $800 < h < 2300$ m

(Fig. 6d). All these features are well captured by the model.

Sea surface $p\text{CO}_2$ validation was also conducted in the nSCS (Fig. S3). This indicates that $p\text{CO}_2$ in the basin is evidently higher than that in coastal areas, particularly close to the PRE and in spring and summer. In the basin, $p\text{CO}_2$ in fall and winter is mostly lower than in spring and summer. The model generally yields comparable patterns to these observations.

Additionally, the model generates a primary production of $444 \text{ mg C m}^{-2} \text{ d}^{-1}$ in spring, $334 \text{ mg C m}^{-2} \text{ d}^{-1}$ in summer, $329 \text{ mg C m}^{-2} \text{ d}^{-1}$ in fall, and $405 \text{ mg C m}^{-2} \text{ d}^{-1}$ in winter (Fig. S4) in the euphotic zone ($h = 0 - 93$ m). These values are close to field observations of $440 \text{ mg C m}^{-2} \text{ d}^{-1}$, $310 \text{ mg C m}^{-2} \text{ d}^{-1}$, $320 \text{ mg C m}^{-2} \text{ d}^{-1}$ and $530 \text{ mg C m}^{-2} \text{ d}^{-1}$ in spring, summer, fall and winter in the SCS basin, respectively (Chen and Chen, 2006) (Fig. S4).

Overall, the model simulates the three-dimensional characteristics of biogeochemical variables and their seasonal variation in the SCS well. In particular, it is able to capture the characteristic differences between the basin and shelves, and between the SCS and the WPS. This provides a high level of confidence in the simulations, an essential requirement for studies of DIC dynamics in the SCS.

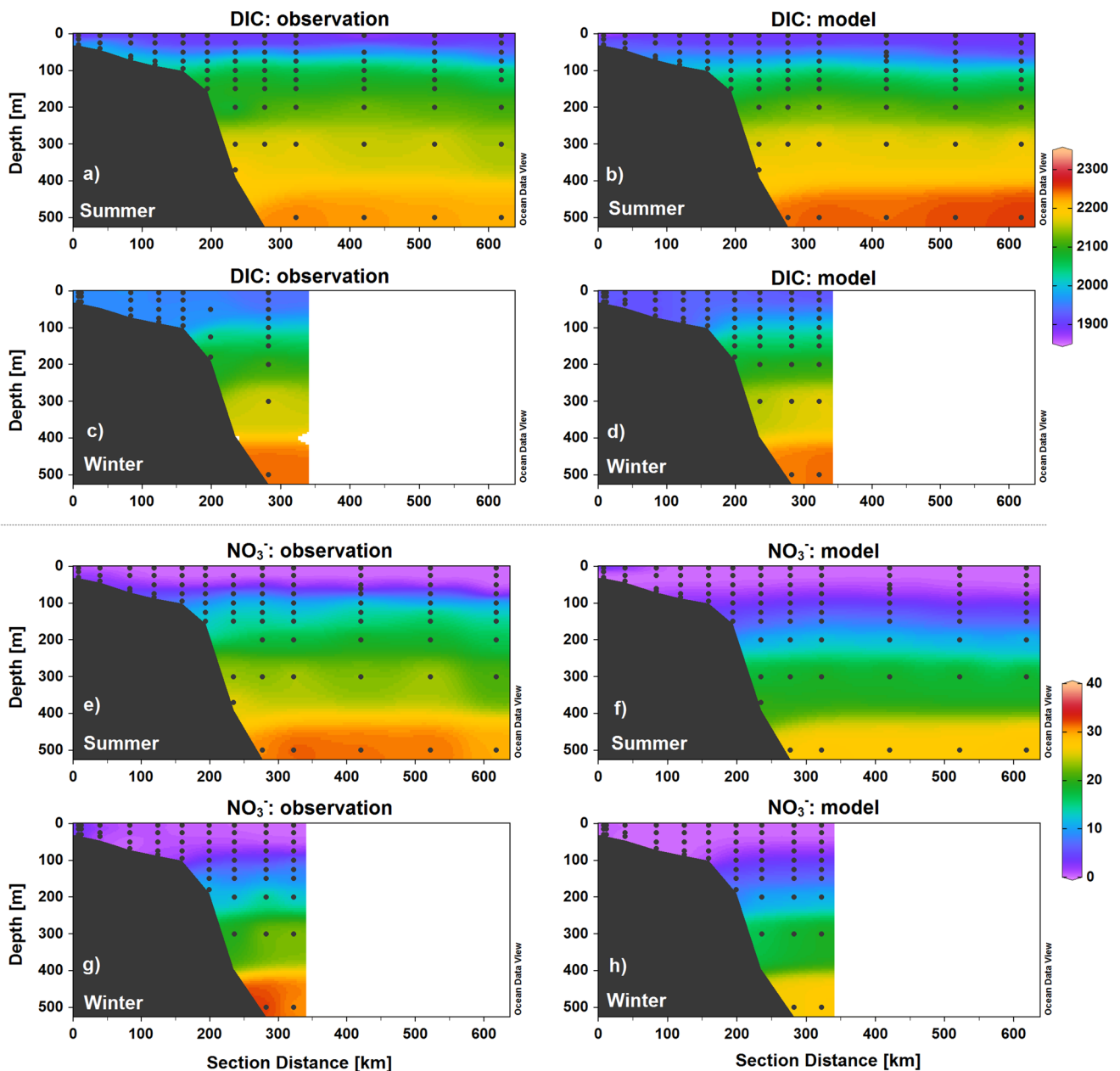


Fig. 5. Depth distributions of dissolved inorganic carbon, DIC (a-d; in $\mu\text{mol kg}^{-1}$) and nitrate, NO_3^- (e-h; in $\mu\text{mol L}^{-1}$) in summer and winter at Section A (see Fig. 1): field observations (left), model simulations (right).

3.2. Seasonal variation in the biogeochemistry of the upper layer

As shown in Fig. 7a, the weekly mean of the mixed layer depth (MLD) is 10 to 30 m, with a maximum in January, an initial minimum in May, and a secondary minimum in October. The weekly mean θ shows an inverse pattern to that of the MLD, with a minimum in January, an initial maximum in May and a secondary maximum in October (Fig. 7b). The weekly mean salinity is 32.8 – 33.6, with higher salinities appearing from February to May and lower salinities appearing in October (Fig. 7c). Weekly mean DIC concentrations within the MLD are highest in February at $\sim 1918 \mu\text{mol kg}^{-1}$ and lowest in October at $\sim 1892 \mu\text{mol kg}^{-1}$ (Fig. 7d). Overall, the seasonal DIC variation within the MLD is consistent with the observations at Sta. SEATS (Tseng et al., 2007). TALK concentrations are 2190 – 2240 $\mu\text{mol kg}^{-1}$, displaying a similar seasonal pattern to salinity (Fig. 7e). The range of mean weekly NO_3^- concentrations is 0.005 – 0.06 $\mu\text{mol L}^{-1}$, showing a similar seasonal pattern to the MLD but an opposite pattern to θ , and

suggesting that vertical transport primarily during winter supplies NO_3^- from deeper layers and increases the NO_3^- concentrations therein (Fig. 7f). Weekly mean DIP concentrations are 0.05 – 0.09 $\mu\text{mol L}^{-1}$, showing higher values from December to May and lower values from August to October (Fig. 7g). Higher DIP concentrations with a lower N/P ratio (< 1.0) suggest that NO_3^- is the main limiting nutrient in the SCS. Weekly mean chlorophyll *a* concentrations show an initial peak (0.3 $\mu\text{g L}^{-1}$) in January and a secondary peak in August, while the lowest concentrations occur in May and October (Fig. 7h).

3.3. DIC spatiotemporal characteristics

The SCS features a CAC circulation structure divided into upper (0–750 m), middle (750–1500 m) and deep (> 1500 m) layers (Gan et al., 2016b). To characterize the upper layer of the CAC, DIC distributions were selected at 0 m (surface), 100 m approximately at the base of the euphotic layer, and at 200 m where the difference in DIC

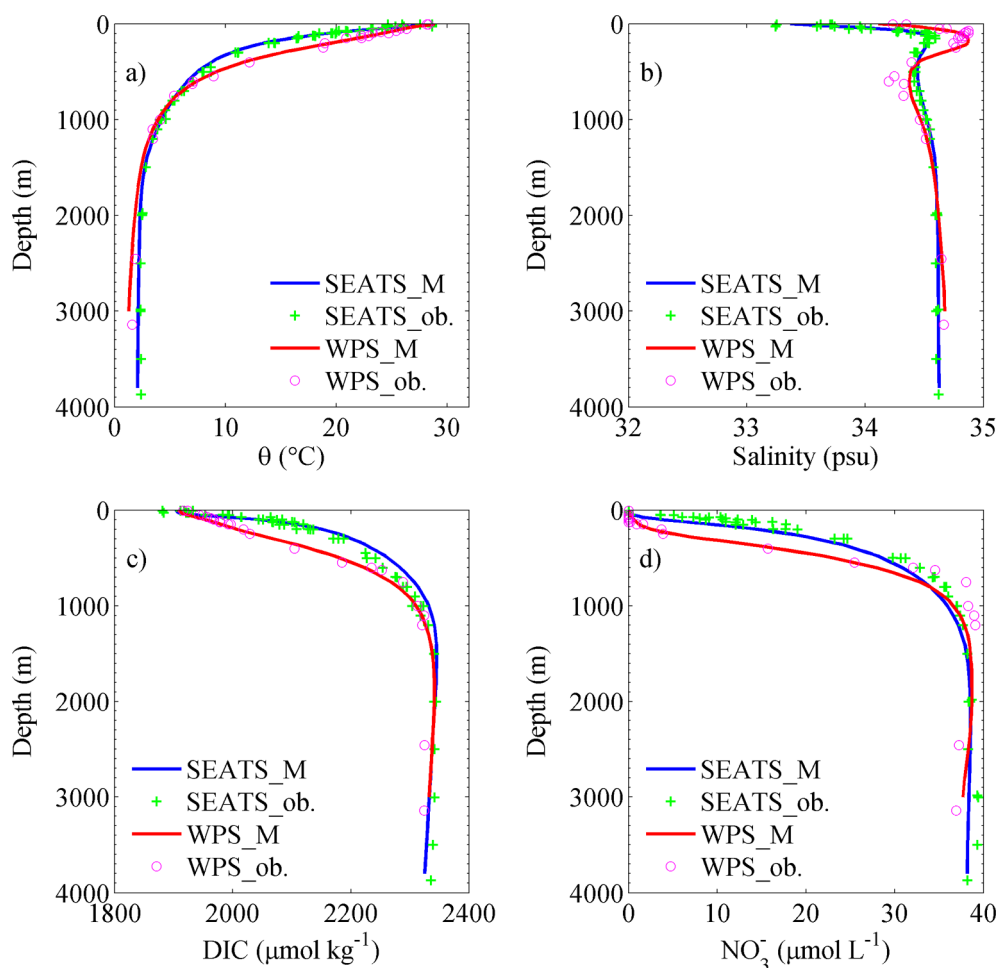


Fig. 6. Depth profiles of (a) potential temperature (θ); (b) salinity; (c) dissolved inorganic carbon (DIC); and (d) nitrate (NO_3^-) at Station SEATS (116°E ; 18°N) in the South China Sea and in the West Philippine Sea, WPS (122.3°E , $20 - 20.5^\circ\text{N}$). The suffixes ‘_ob.’ and ‘_M’ denote field observations and model simulations, respectively.

between the SCS and the WPS reaches its maxima. Those distributions at 1000 m and 2500 m were chosen to represent the middle and deep layers, respectively.

Upper 200 m

At the surface, the model shows pronounced variation in spatial and seasonal DIC concentrations in the SCS (Fig. 8a–d). In summer, these are obviously lower in the northern shelf extending from the Pearl River mouth to the southwestern reaches of the Taiwan Strait, at the Mekong River mouth extending eastward ~ 200 km, and in the Gulf of Thailand close to the north and west coasts (Fig. 8b). These patchy distributions show similar patterns to those of salinity (Fig. S5), suggesting that freshwater inputs, primarily from river runoff, evidently reduce DIC concentrations in these regions. During winter, DIC concentrations on the northern shelf increase evidently (Fig. 8d) and the low-DIC region appearing off the Mekong River mouth moves westward to coastal areas, near the Ca Mau Peninsula. A high-DIC patch is found in the southwest basin ($108 - 114^\circ\text{E}$; $4 - 12^\circ\text{N}$; Fig. 8d), where counter-clockwise circulation favoring upwelling was previously reported (Liu and Gan, 2017) and potentially supplied higher DIC concentrations from the subsurface to the upper layer. In the basin, winter DIC concentrations are generally higher than in summer (Fig. 8d), corresponding to lower temperatures and higher salinities (Figs. S5 and S6). This suggests that vertical transport during the winter potentially supplies DIC from subsurface to surface waters and increases DIC concentrations therein. This result is consistent with findings of prior studies (Chou et al., 2005; Tseng et al., 2007). Except for slightly different values and spatial patterns, DIC distributions in spring and fall resemble

those in winter and summer, respectively. Furthermore, throughout the entire Gulf of Thailand DIC concentrations, particularly close to coastal areas, are evidently lower than in the SCS basin (by up to $200 \mu\text{mol kg}^{-1}$) year-round (Fig. 8a–d).

At 100 m, a salient feature is that DIC concentrations in the northeast SCS are lower than in the central basin throughout the year (Fig. 8e–h). As DIC concentrations in the WPS are 100 to $150 \mu\text{mol kg}^{-1}$ lower than in the SCS, lower DIC concentrations in the northeast SCS should primarily be attributed to the dilution effect of the Kuroshio intrusion. Additionally, DIC concentrations in the central basin are mostly higher than those close to the slope (Fig. 8e–h). Since upper layer circulation in the SCS is cyclonic (Gan et al., 2016a, b; Liu and Gan, 2017), favoring upwelling in the central basin, these higher DIC concentrations in the basin are attributable to the DIC supplied from the deep layer to the upper layer.

In summer, DIC concentrations to the east, off central Vietnam ($109.5 - 112^\circ\text{E}$; $10 - 15^\circ\text{N}$) are 50 to $80 \mu\text{mol kg}^{-1}$ higher than in the surrounding regions (Fig. 8f). In this area, θ is 2.0 to 3.0°C lower and σ_θ is $\sim 0.6 \text{ kg m}^{-3}$ higher than that in surrounding waters (Fig. S5), and circulation is cyclonic, suggesting that a cyclonic cold eddy (Gan and Qu, 2008) provides colder, denser and higher-DIC water from the deeper layer to the upper layer. This eddy persists until fall, with its area extending slightly to the east (Fig. S5). To the south of the eddy, a low-DIC patch associated with anticyclonic circulation is shown (Fig. 8f), where θ is relatively higher and σ_θ is relative lower than that in surrounding waters (Fig. S5). This suggests that an anticyclonic warm eddy reduces DIC concentrations in this area presumably due to

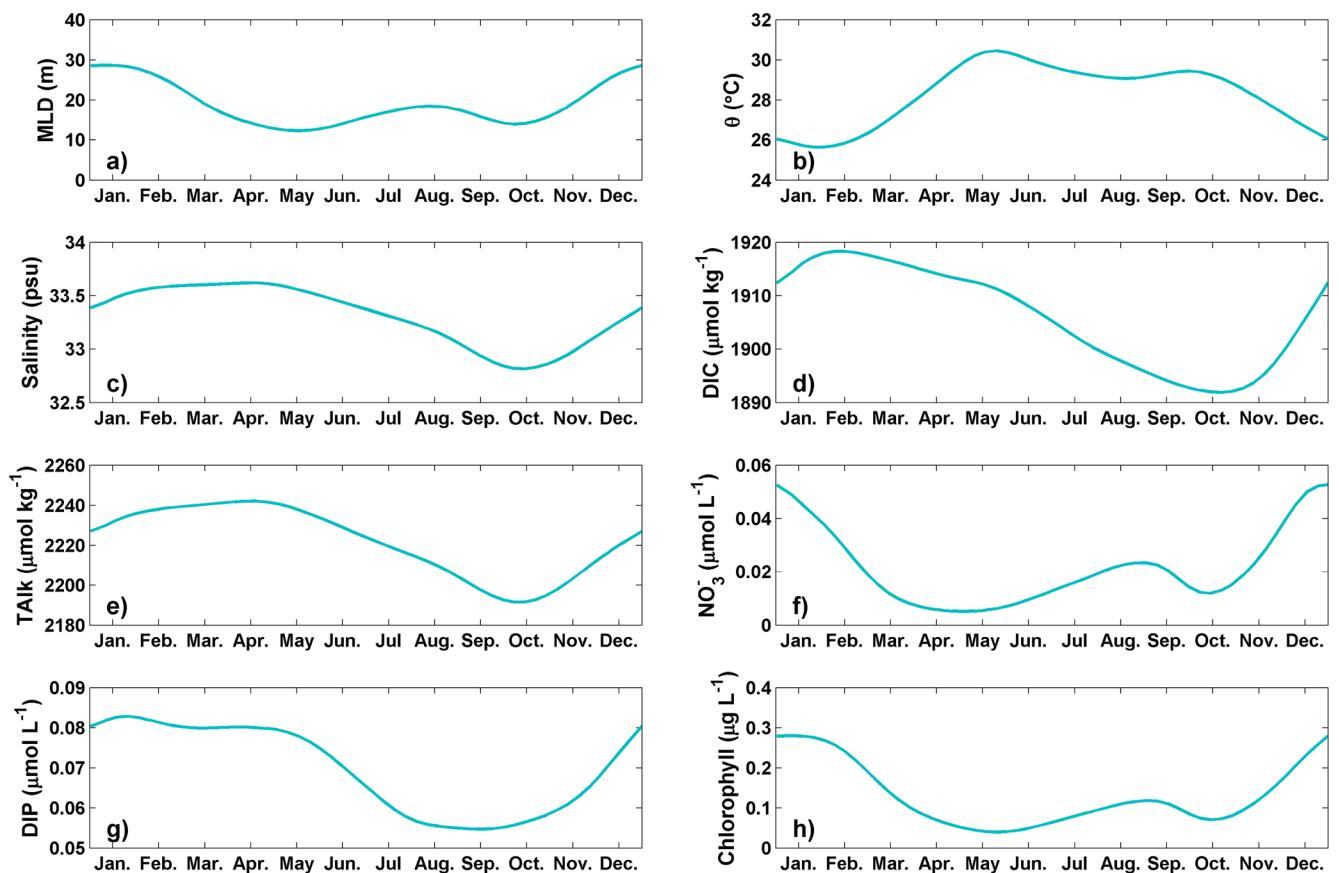


Fig. 7. Annual weekly mean of (b) potential temperature (θ); (c) salinity; (d) dissolved inorganic carbon, DIC; (e) total alkalinity, TAlk; (f) nitrate, NO_3^- ; (g) dissolved inorganic phosphate, DIP; and (h) chlorophyll *a* in (a) mixed layer depth (MLD) in the South China Sea basin.

depression of the isopycnal surface.

In winter, DIC concentrations are $> 2060 \mu\text{mol kg}^{-1}$ in the central basin extending from the southwest Luzon Strait to southwest SCS (Fig. 8h). In contrast, DIC concentrations ranging from 1900 to $2020 \mu\text{mol kg}^{-1}$ are confined to a narrow band 40 to 100 km wide along the northern, western and southern basin margins, which are 100 to $180 \mu\text{mol kg}^{-1}$ lower than in the central basin (Fig. 8h). Correspondingly, θ and σ_θ in the basin margins are $\sim 2.0^\circ\text{C}$ higher and $\sim 1.0 \text{ kg m}^{-3}$ lower than in the central basin, respectively (Fig. S6), suggesting that downwelling carries low-DIC water from the upper layer to the deeper layer. The Kuroshio intrusion may also contribute to this feature, particularly in the northeast where it is indicated by higher salinity and westward currents (Figs. 8 and S6). The DIC distributions in spring and fall are generally intermediate between summer and winter.

At 200 m, DIC distributions generally show similar patterns to those at 100 m (Fig. 8i-l), other than that spatial variation, particularly in the sSCS, is largely reduced. The most pronounced feature is that DIC concentrations in the northeast basin are evidently lower than in the central and southern basins (by up to $70 \mu\text{mol kg}^{-1}$), evidencing DIC dilution by Kuroshio intrusion. At 200 m, differences in DIC concentrations between the SCS and the WPS reach a maximum of $\sim 207 \mu\text{mol kg}^{-1}$. In winter, the low DIC band along basin margins is still present, but with a largely reduced strength.

Deep basin

Below 200 m, the seasonal variation in DIC is small compared to that in the upper layer (Fig. 8m-t). At 1000 m, higher DIC concentrations (by up to $20 \mu\text{mol kg}^{-1}$) were found in the southern and western regions relative to those in the northeast (Fig. 8m-p). This distinct pattern is also shown at other intermediate horizons (data not shown) and supported by observations (Fig. S7). We speculate that these higher DIC regimes are associated with degradation of sinking particles

originating from upper ocean biotic production (Tan and Shi, 2009), in conjunction with longer water residence time in these areas (Liu and Gan, 2017). Indeed, these areas are also characterized by a relatively low dissolved oxygen (DO) concentration as reported by Li and Qu (2006). The DIC distribution at 2500 m resembles that at 1000 m, and DIC concentrations in the sSCS are only slightly higher than in the northeast near the Luzon Strait (Fig. 8q-t).

Overall, DIC concentrations increase evidently from the WPS to the nSCS, e.g., by up to $140 \mu\text{mol kg}^{-1}$ at 200 m (Fig. 6c and 9). In the SCS they primarily display a north to south gradient, particularly at > 100 m. If the basin is divided into a northern and southern sectors with a boundary at 9°N (Liu and Gan, 2017), DIC concentrations in the southern basin are 0 to $20 \mu\text{mol kg}^{-1}$ higher than in the northern basin in the upper 1400 m (Fig. 9).

3.4. DIC exchange fluxes with adjacent seas and shelves

The spatial and seasonal variation of DIC concentrations are largely determined by DIC exchanges with adjacent seas via a suite of straits, i.e., Luzon, Mindoro and Balabac, Taiwan and Karimata Straits. The DIC flux (F_c) is calculated by

$$F_c = \int_0^s (u \times c) ds \quad (1)$$

where, u is the current velocity normal to a given cross section s , c is the DIC concentration, and S is the total integrated length or area. The outflow velocity is defined as positive and the inflow velocity as negative. The overbar denotes time averaging.

The DIC fluxes shown in Figs. 10 and 12a are horizontally integrated along the width of the strait in order to show the profiles of DIC fluxes

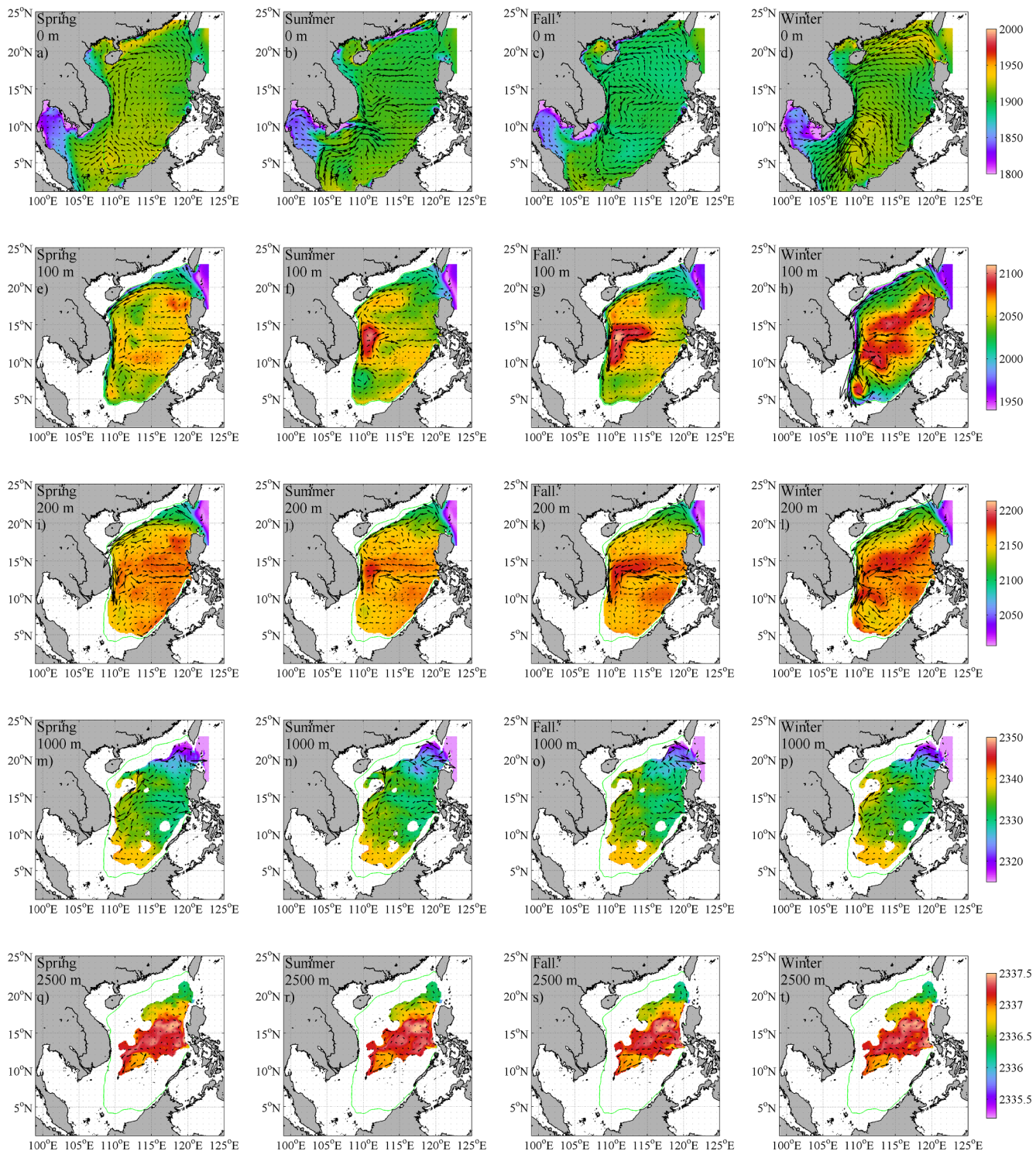


Fig. 8. Spatial distributions and seasonal variation of dissolved inorganic carbon (DIC) at 0 m (a-d); 100 m (e-h); 200 m (i-l); 1000 m (m-p); and 2500 m (q-t) in summer and winter (in $\mu\text{mol kg}^{-1}$). The black arrows denote the horizontal velocity vectors of the model simulation.

both across different straits and the 100 m isobath. The DIC fluxes shown in Fig. 11 are integrated both horizontally and vertically to show the total fluxes across straits.

3.4.1. Fluxes across the straits

Fluxes across the Luzon Strait

A boundary of 120.9°E was selected to present the DIC fluxes across the Luzon Strait. Fluxes of DIC display evident seasonal variation in the upper 100 m (Fig. 10a), and are mostly negative, suggesting a DIC

influx, whereas a DIC outflux only occurs in the upper 35 m in summer. Annually, the DIC influx is $3.5 \times 10^6 \text{ mol s}^{-1}$ in the upper 100 m (Fig. 11). Between 100 and 600 m, DIC fluxes during all seasons increase with depth and remain negative, with an annual average of $9.2 \times 10^6 \text{ mol s}^{-1}$ (Fig. 11), suggesting a year-round DIC influx to the SCS via the Luzon Strait. Seasonally, the DIC influx peaks in winter and is lowest in summer (Fig. 10a). As DIC concentrations in the WPS are evidently lower than in the SCS (Fig. 6c), the influx of DIC at the Luzon Strait can greatly dilute DIC concentrations in the SCS.

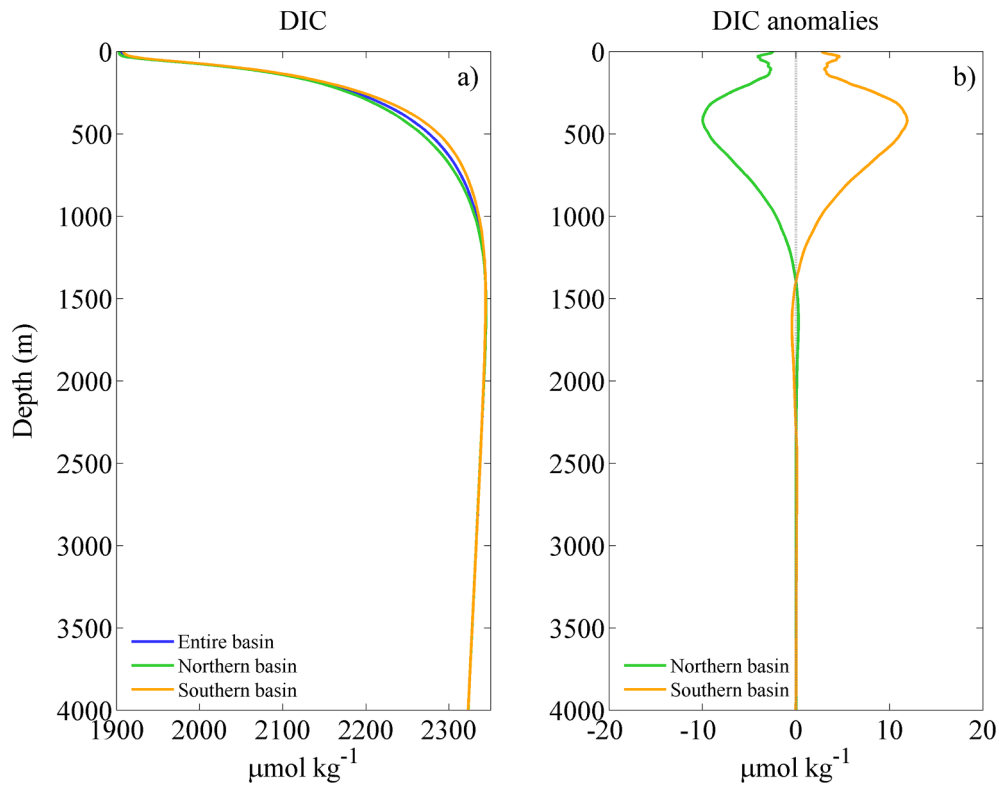


Fig. 9. Depth profiles of mean dissolved inorganic carbon, DIC (a) and their anomalies, in $\mu\text{mol kg}^{-1}$ (b) in the entire basin, and in northern and southern basins, with a boundary at 9°N .

The intermediate layer ($600\text{ m} < h < 1600\text{ m}$), primarily exhibits a DIC outflux with maxima in spring and minima in summer (Fig. 10a). The annual mean outflux is $3.3 \times 10^6\text{ mol s}^{-1}$ (Fig. 11), i.e., about a fourth of the DIC influx in the upper 600 m. In deeper layers ($>1600\text{ m}$), the seasonal variation of DIC fluxes is small, with an annual influx of $1.8 \times 10^6\text{ mol s}^{-1}$ (Fig. 11). Overall, DIC fluxes at the Luzon Strait display a ‘sandwich’ structure, with an influx in the upper layer ($<600\text{ m}$) and deep layer ($>1600\text{ m}$) and an outflux in the

intermediate layer (600 to 1600 m), which is qualitatively similar to the horizontal influx-outflux-influx flow structure previously described at the Luzon Strait (Gan et al., 2016a). It is noteworthy that the DIC fluxes estimated in the present study differ partially from those reported by Chen et al. (2006). Their estimates are evidently lower than those obtained in this study in the upper layer ($1.9 \times 10^6\text{ mol s}^{-1}$; $< 350\text{ m}$), but higher than those obtained in the present study in the intermediate ($4.3 \times 10^6\text{ mol s}^{-1}$ at $350 - 1350\text{ m}$) and deep layers ($2.8 \times 10^6\text{ mol s}^{-1}$ at $1350 - 4000\text{ m}$).

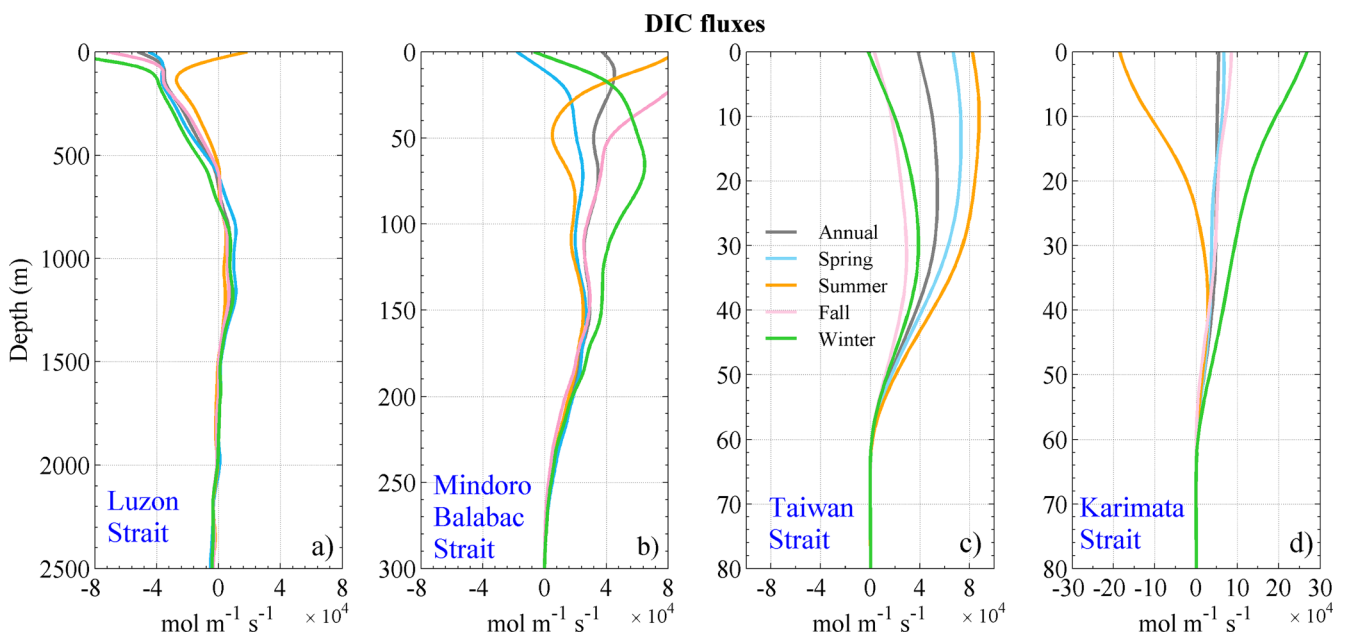


Fig. 10. Depth profiles of dissolved inorganic carbon (DIC) fluxes at the Luzon (a), Mindoro and Balabac (b), Taiwan (c) and Karimata Straits (d) (see Fig. 1). The fluxes are integrated in a horizontal coordinate along the width of the strait. The different colors denote the fluxes as annual and/or seasonal means.

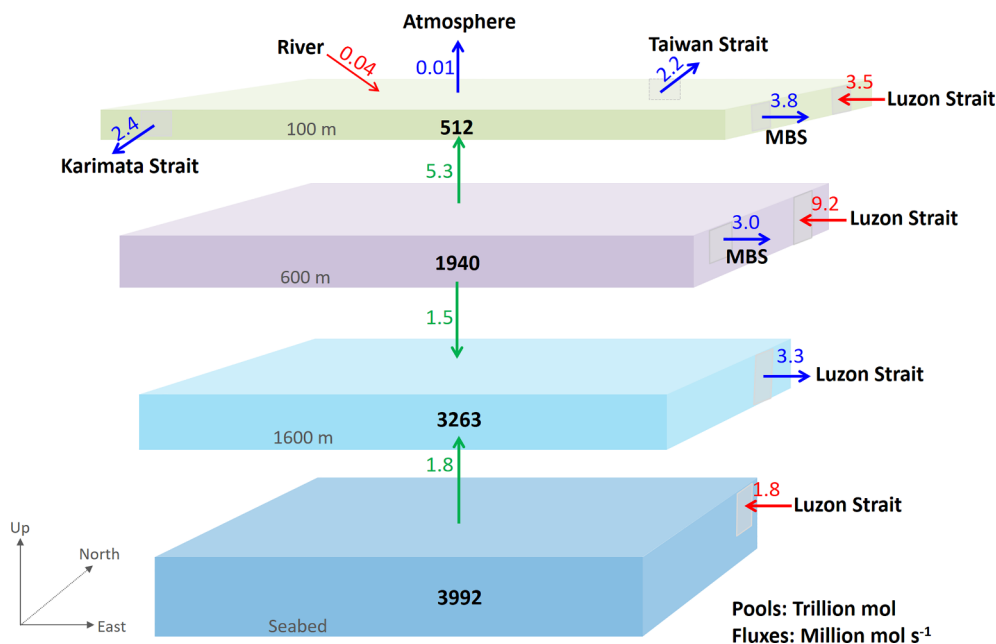


Fig. 11. Schematic diagram of dissolved inorganic carbon (DIC) transport at the Luzon, Taiwan, Mindoro and Balabac (MBS), and Karimata Straits, and from rivers in the South China Sea. The red (blue) text and arrows denote net influxes (outfluxes); the green text and arrows denote vertical fluxes; the black number denotes the DIC pool size. (For interpretation of the references to colours in this figure legend, the reader is referred to the web version of this paper.)

s^{-1} at > 1350 m), which is attributable to the different depth ranges and water fluxes applied in their study.

Fluxes across the Mindoro and Balabac Strait

The summation of DIC fluxes along 121.1°E (11.8°N – 13.8°N), 11.8°N (120.1°E – 121°E), 119.8°N (10.6°N – 11.6°N) and 117.3°E (6.9°N – 8.1°N) was selected to represent the DIC fluxes at the Mindoro and Balabac Strait (Fig. 10b). In different seasons, the DIC fluxes are mostly positive, suggesting a DIC outflux from the SCS to the Sulu Sea. In the upper 30 m, the DIC fluxes show maxima in fall and minima in spring. At depths > 40 m, the DIC outflux is maximal in winter and minimal in summer. The annual mean DIC outflux is $3.8 \times 10^6 \text{ mol s}^{-1}$ in the upper 100 m and $3.0 \times 10^6 \text{ mol s}^{-1}$ between 100 m and 600 m (Fig. 11). This result differs from those in previous studies that show a DIC influx at the Mindoro and Balabac Strait (e.g., Chen et al., 2006). This is unlikely based on the overall circulation (Gan et al., 2016a) and water mass pathways (Liu and Gan, 2017) in the SCS.

Fluxes across the Taiwan Strait

A boundary at 24.1°N (117.6°E – 120.4°E) was used to represent DIC fluxes across the Taiwan Strait (Fig. 10c). Results primarily show a DIC outflux from the entire water column, with maxima in summer and minima in fall and winter. Annually, the DIC outflux is $2.2 \times 10^6 \text{ mol s}^{-1}$, only slightly lower than the DIC outflux across the Mindoro and Balabac Strait in the upper 100 m (Fig. 11). The estimated DIC fluxes are evidently greater than the previous estimate of $0.68 \times 10^6 \text{ mol s}^{-1}$ at the Taiwan Strait (Chen et al., 2006), which is attributable to the water fluxes of 0.2 to 0.5 SV (1 SV = $10^6 \text{ m}^3 \text{ s}^{-1}$) estimated by these authors, i.e., much lower than the estimate of 1.2 SV by Gan et al. (2016a).

Fluxes across the Karimata Strait

A boundary at 1.7°N (103.9°E – 109.5°E) was selected to represent the DIC fluxes across the Karimata Strait (Fig. 10d). Results primarily indicate a DIC outflux with influx solely found in the upper 124 m in

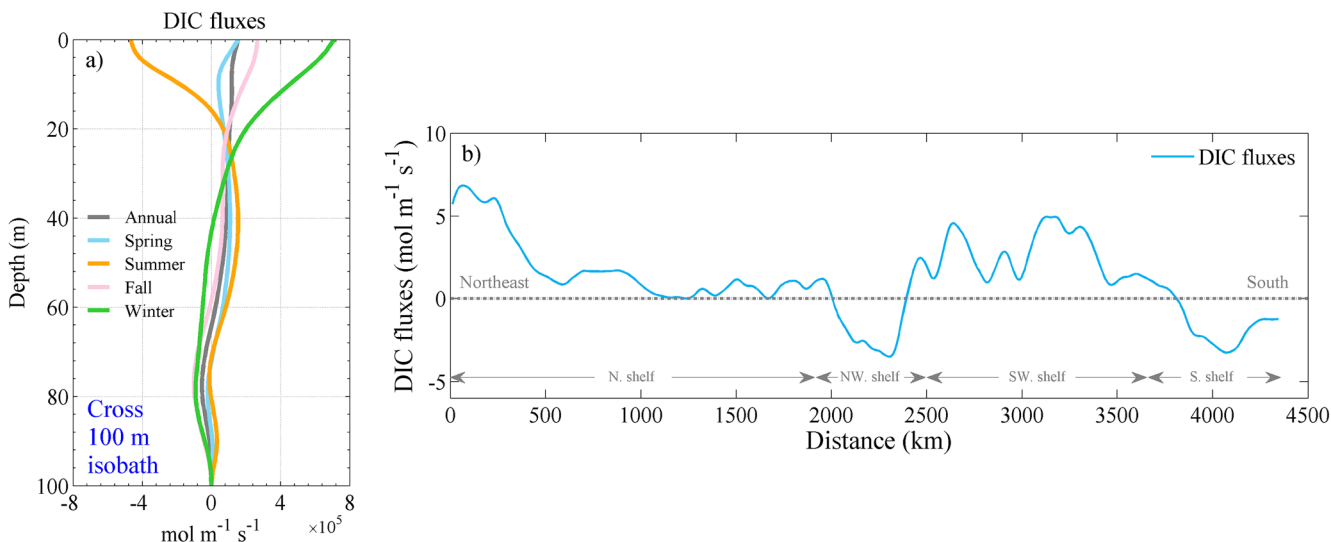


Fig. 12. (a) As in Fig. 10, seasonal depth profiles of dissolved inorganic carbon (DIC) fluxes across the 100 m isobath; (b) vertically integrated DIC fluxes across the 100 m isobath around the South China Sea basin; the x-axis denotes the distance from the northeastern shelf close to southwest Taiwan, extending to the southern shelf close to north Borneo in a counterclockwise direction (Fig. S8). ‘N shelf’, ‘NW shelf’, ‘SW shelf’ and ‘S shelf’ denote the northern, northwestern, southwestern and southern shelves, respectively.

summer. Fluxes of DIC show evident seasonal variation with maxima found in winter and minima in summer. DIC fluxes in spring and fall approach the annual mean. On an annual basis, the DIC outflux is $2.4 \times 10^6 \text{ mol s}^{-1}$ (Fig. 11), comparable to that across the Taiwan Strait (Fig. 11). The DIC outflux across the Karimata Strait estimated in the present study is twice that of $1.1 \times 10^6 \text{ mol s}^{-1}$ estimated by Chen et al. (2006).

In the upper 100 m water column, the summation of DIC outflux across the Mindoro and Balabac, Taiwan and Karimata Straits is twice as large as the DIC influx at the Luzon Strait (Fig. 11), suggesting that an additional DIC source, likely supplied from depth, is required to balance the DIC budget. Indeed, the DIC vertical flux is $5.3 \times 10^6 \text{ mol s}^{-1}$ at 100 m (Fig. 11; Sec. 3.5), which roughly balances the above deficit in the DIC influx.

3.4.2. Shelf-basin exchanges

The DIC fluxes across the 100 m isobath (Fig. S8) may largely reflect shelf-basin exchanges. The positive DIC fluxes are defined as an outflux, representing DIC transport from the basin to the shelf, and vice versa (Fig. 12a). They show maximum DIC fluxes in the upper 25 m in winter and depths > 25 m in summer. In contrast, DIC fluxes are negative in the upper 15 m in summer, suggesting a DIC influx. Negative DIC fluxes also occur at depths > 40 m in winter and > 60 m in fall. Annually, the DIC flux across the 100 m isobath is $4.8 \times 10^6 \text{ mol s}^{-1}$, suggesting net transport of DIC from the basin toward the shelves. This value is slightly higher (by 0.5 %) than the summation of the DIC outflux at the Taiwan and Karimata Straits (Fig. 11), suggesting that most of these DIC fluxes across the 100 m isobath contribute to the DIC outflow across the Taiwan and the Karimata Straits.

Vertically integrated DIC fluxes along the 100 m isobath are shown in Fig. 12b. It is apparent that DIC fluxes are mostly positive, reflecting DIC transport from the basin to the northern and southwestern shelves. In contrast, DIC fluxes are negative, reflecting those from northwestern and southern shelves to the basin.

3.5. DIC vertical fluxes

Horizontally integrated DIC vertical fluxes over the SCS basin are shown in Fig. 13. Vertical fluxes in different seasons display similar patterns. Annually, DIC vertical fluxes increase from $\sim 0.0 \times 10^6 \text{ mol s}^{-1}$ at the surface to a maximum of $5.8 \times 10^6 \text{ mol s}^{-1}$ at 65 m, reflecting upward transport of DIC (Fig. 13). Fluxes then decrease rapidly

to negative values of $(-1.5 \text{ to } 0.0) \times 10^6 \text{ mol s}^{-1}$ at 400 to 1100 m, suggesting downward transport of DIC. At depths > 1100 m, DIC vertical fluxes increase to attain a maximum of $\sim 1.9 \times 10^6 \text{ mol s}^{-1}$ at 1500 to 1800 m, and then decrease to $\sim 0.0 \times 10^6 \text{ mol s}^{-1}$ at > 2700 m. The calculated DIC vertical fluxes are consistent with the water fluxes reported in this (Fig. S9) and previous studies (Fang et al., 2009; Liu and Gan, 2017), suggesting that physical dynamics largely control DIC vertical transport.

Seasonally, maximum and minimum DIC vertical fluxes in the upper 400 m occur in winter and summer, respectively (Fig. 13). Below 400 m, maximum values occur in the fall, whereas minimum values occur in spring. The seasonal variation of DIC vertical fluxes is consistent with the water vertical fluxes (Fig. S9), suggesting that adjustment of the physical dynamics largely controls the DIC vertical flux on a seasonal timescale.

Overall, the combined effects of downward transport of DIC at 400 – 1100 m and upward DIC transport at > 1100 m provide the DIC outflow sources to the WPS in the intermediate layer via the Luzon Strait (Fig. 11). This agrees with the three-dimensional water mass transport in the SCS described by Liu and Gan (2017). In addition, DIC downward transport at 400 – 1100 m should constrain the DIC upward transport from the deep to the upper layer. Thus, DIC dynamics in the upper SCS should primarily be influenced by the horizontal DIC transport from the Kuroshio intrusion rather than through the vertical transport from the deep layer (see additional discussion in Section 4.2).

Table 1 summarizes the seasonal variation in DIC horizontal fluxes integrated in the upper 100 m at various straits, and DIC vertical fluxes at 100 m. It shows that the Luzon Strait makes the greatest contribution to the horizontal DIC fluxes in the SCS. In addition to vertical fluxes, these two situations provide the major sources of DIC to the upper 100 m. Both exhibit similar seasonal trends, with the lowest influxes occurring in summer and the highest in winter. In contrast, the DIC fluxes are mostly positive, indicating DIC export from the SCS, at the Mindoro and Balabac, Taiwan and Karimata Straits. Fluxes of DIC show similar seasonal trends at the Mindoro and Balabac and Karimata Straits, with the lowest outflux found in summer and the highest in winter. Through the Taiwan Strait, the highest and lowest DIC outfluxes occur in summer and winter respectively.

4. Discussion

4.1. DIC budget and biogeochemical modifications

Analysis of the DIC budget was conducted to allow investigation of DIC dynamics. The relationship of different DIC terms in the model are as follows

$$\text{DIC}_t = \text{HADV} + \text{VADV} + \text{hdiff} + \text{Vdiff} + \text{DIC}_{\text{prod}} + \text{DIC}_{\text{Zmeta_ex}} + \text{DIC}_{\text{Dremin}} + \text{DIC}_{\text{CO}_2\text{-air-sea}} \quad (2)$$

where, DIC_t is the time rate of change of the DIC inventory, and HADV and VADV are the horizontal and vertical advection terms, respectively. In model, the HADV (VADV) term is the divergence of the horizontal (vertical) advective fluxes. The hdiff and Vdiff are the horizontal and vertical diffusion term, respectively; DIC_{prod} is the production term; $\text{DIC}_{\text{Zmeta_ex}}$ refers to zooplankton metabolism and excretion term; $\text{DIC}_{\text{Dremin}}$ indicates the detritus remineralization term, and $\text{DIC}_{\text{CO}_2\text{-air-sea}}$ is the air-sea CO_2 exchange term. On the right-hand side of Eq. (2), a positive term indicates an increase in DIC_t , and vice versa. The terms listed in Eq. (2) are individually integrated from the corresponding model output at the model grid, both horizontally over the SCS basin and vertically in the euphotic zone, middle and deep layers, respectively. The terms are then averaged over time. It is worth noting that the corresponding HADV and VADV terms from the model output are “s-coordinates”, rather than horizontal or vertical coordinates. Here, the sum of DIC horizontal fluxes in different boundaries (i.e., Luzon,

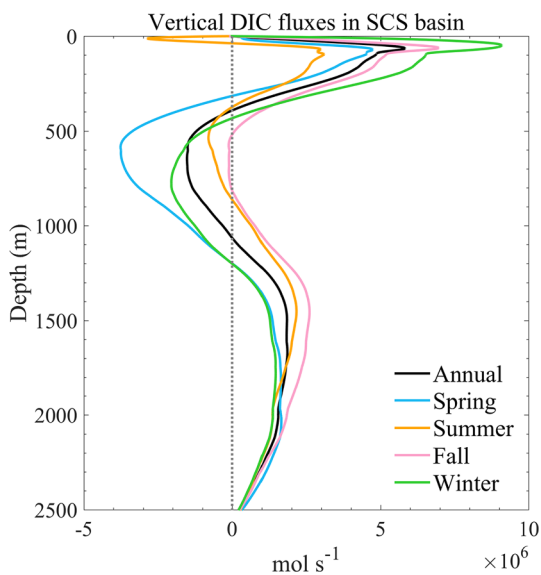


Fig. 13. Seasonal depth profiles of vertical dissolved inorganic carbon (DIC) fluxes in the South China Sea basin.

Table 1

Seasonal variation in DIC horizontal fluxes integrated in the upper 100 m in the Luzon, Mindoro and Balabac, Taiwan and Karimata Straits (see Fig. 1), and the DIC vertical fluxes at 100 m (in mol s⁻¹). The negative sign for horizontal fluxes denotes the influxes to the SCS and vice versa. The positive sign for vertical fluxes denotes upward fluxes.

Season	Luzon Strait	Mindoro & Balabac Strait	Taiwan Strait	Karimata Strait	Vertical
Spring	-3.0 × 10 ⁶	2.1 × 10 ⁶	2.9 × 10 ⁶	2.7 × 10 ⁶	4.5 × 10 ⁶
Summer	-1.0 × 10 ⁶	2.6 × 10 ⁶	3.5 × 10 ⁶	-1.7 × 10 ⁶	3.1 × 10 ⁶
Fall	-2.9 × 10 ⁶	4.8 × 10 ⁶	1.4 × 10 ⁶	2.0 × 10 ⁶	5.2 × 10 ⁶
Winter	-6.7 × 10 ⁶	5.3 × 10 ⁶	1.2 × 10 ⁶	6.5 × 10 ⁶	6.5 × 10 ⁶

and Mindoro and Balabac Straits, and across the 100 m isobath) are calculated, which are in the ‘u’ or ‘v’ grid and in horizontal coordinates. This estimates the divergence of the horizontal advective fluxes (HADV term) in the SCS basin. The VADV term is residually computed according to Eq. (2).

If 1 % of the surface irradiance is used as a criterion, the mean euphotic zone depth in the SCS basin is 93 m in spring, 90 m in summer, 94 m in fall, and 95 m in winter. Given that the seasonal variation of the mean euphotic zone depth is small, and to allow a consistent comparison, a mean value of 93 m was selected as the euphotic zone depth to calculate the DIC budget.

The seasonal variation in the DIC budget based on Eq. (2) terminologies in the euphotic zone of the SCS basin is shown in Fig. 14. The DIC_t sign is negative in spring and summer, indicating a decrease in DIC inventories. The pattern is reversed in fall and winter. The seasonal DIC_t pattern agrees with the variation in DIC concentration in the MLD (Fig. 7). The HADV term is negative in the euphotic zone throughout the year, tending to decrease DIC inventories. In contrast, the VADV term is positive year-round, tending to increase DIC inventories. The absolute values of HADV and VADV are greater (by > 6.5×) than the other terms, suggesting that they are the dominant DIC terms in the euphotic zone. Their signs are opposite, however, so they tend to neutralize each other. Seasonally, the VADV (HADV) term shows a minimum (maximum) value in summer and a maximum (minimum) value in winter.

The DIC_{prod} term is the primary biotic removal term. It is minimal in spring and maximal in summer. The DIC_{Dremin} term, the primary biotic

addition term, attains a maximum value in spring and a minimum value in fall. Compared to the summer, a higher DIC_{prod} and an equivalent DIC_{Dremin} occurred in winter, suggesting a higher net community production (NCP). This is in agreement with results of Chen (2005), who stated that higher rates of new production were generally observed in winter. The DIC_{CO₂air-sea} term is negative from spring to fall, and tends to decrease DIC concentrations, suggesting that there is a CO₂ source to the atmosphere, but it exhibits a reverse pattern in winter.

In the middle and deep layers, the HADV and VADV terms are ~2 orders of magnitude greater than the DIC_t, and 3 to 5 orders of magnitude greater than the DIC_{Dremin} (Figs. S10 and S11), thus dominating the DIC budget. The DIC_t, both in the middle and deep layers, shows a decrease in DIC inventories in spring and summer, but an increase in fall and winter.

To discriminate between the effects of physical and biogeochemical processes on changes in the DIC inventory, the individual constitutive terms were grouped into four components, i.e., DIC_t, indicative of a DIC inventory change; a physical transport term (DIC_{physics} = HADV + VADV + hdiff + Vdiff), indicative of combined DIC horizontal fluxes via various straits and DIC vertical fluxes; a biotic term (DIC_{bio} = DIC_{prod} + DIC_{Zmeta_ex} + DIC_{Dremin}), and DIC_{CO₂air-sea} indicative of net DIC consumption and air-sea CO₂ exchange, respectively. Thus, Eq. (2) can be rewritten as

$$DIC_t = DIC_{physics} + DIC_{bio} + DIC_{CO_2_{air-sea}} \tag{3}$$

These grouped terms are shown in Table 2. In spring, a negative DIC_t suggests a DIC inventory decrease, with DIC_{physics} and DIC_{CO₂air-sea}

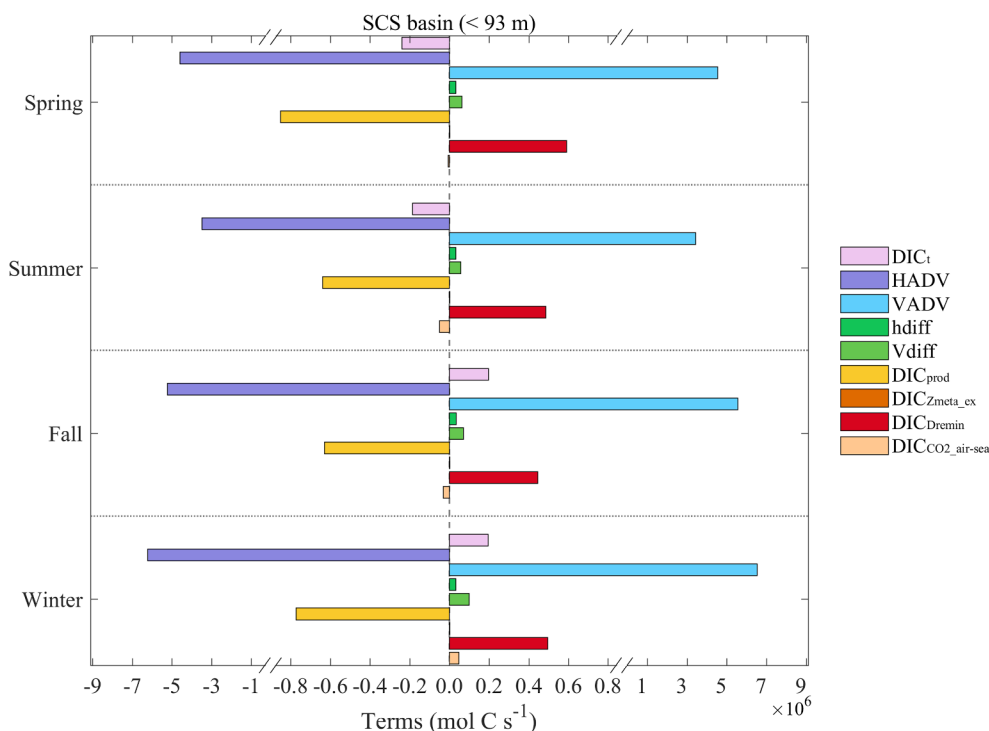


Fig. 14. Seasonal dissolved inorganic concentration (DIC) budget in the euphotic zone (0 to 93 m) of the South China Sea (SCS) basin. ‘DIC_t’, ‘HADV’, ‘VADV’, ‘hdiff’, ‘Vdiff’, ‘DIC_{prod}’, ‘DIC_{Zmeta_ex}’, ‘DIC_{Dremin}’, and ‘DIC_{CO₂air-sea}’ denote the time rate of change of the DIC inventory, horizontal and vertical advection terms, horizontal and vertical diffusion terms, DIC production term, zooplankton metabolism and excretion term, detritus remineralization term, and air-sea CO₂ exchange term, respectively.

Table 2

Grouped DIC terms, DIC_t , $DIC_{physics}$, DIC_{bio} and $DIC_{CO_2,air-sea}$ (see text for abbreviations), in the euphotic zone of the South China Sea basin (in mol s^{-1}) by season. Percent values in brackets are the contributions of $DIC_{physics}$, DIC_{bio} and $CO_2_{air-sea}$ to the total rate of DIC change (DIC_t).

Season	DIC_t	$DIC_{physics}$	DIC_{bio}	$DIC_{CO_2,air-sea}$
Spring	-2.41×10^5	2.32×10^4 (-10 %)	-2.61×10^5 (108 %)	-7.06×10^3 (3 %)
Summer	-1.86×10^5	1.94×10^4 (-10 %)	-1.55×10^5 (84 %)	-5.05×10^4 (27 %)
Fall	1.97×10^5	4.13×10^5 (210 %)	-1.85×10^5 (-94 %)	-3.18×10^4 (-16 %)
Winter	1.93×10^5	4.31×10^5 (223 %)	-2.78×10^5 (-144 %)	4.64×10^4 (24 %)

contributing -10 % and 3 % of the DIC_t , respectively. These contributions play less important roles, while DIC_{bio} contributes 108 % of the DIC_t . This implies that the reduced DIC inventory in spring is mainly caused by net DIC consumption (Table 2). In summer, it displays a similar pattern to that in spring, except for $DIC_{CO_2,air-sea}$, which contributes 27 % of the DIC_t . This pattern is reversed in fall and winter compared to that in spring and summer (Table 2). In turn, a positive DIC_t suggests an increase in the DIC inventory. The $DIC_{physics}$ in fall (winter) is $\sim 20 \times$ greater than in spring and summer, and contributes 210 % (223 %) of the DIC_t , dominating the DIC inventory increase. As the HADV term is a DIC sink, the DIC vertical transport, i.e., VADV term, plays a dominant role in the DIC inventory increase in these two seasons (Fig. 14). The DIC_{bio} contributes -94 % (-144 %) of the DIC_t in fall and winter, respectively, and tends to lower the DIC inventory, playing a secondary role in its effect on the DIC_t . The $DIC_{CO_2,air-sea}$ contributes -16 % and 24 % of the DIC_t in fall and winter, respectively. Annually, the $DIC_{physics}$ and DIC_{bio} terms play important, roughly equivalent roles on the variation of the DIC inventory in the euphotic zone.

The DIC_{bio} term corresponds to the NCP and/or particulate organic carbon (POC) export in the euphotic zone. It is 11.2, 6.7, 8.0 and 12.0 $\text{mmol C m}^{-2} \text{d}^{-1}$ in spring, summer, fall and winter, respectively. This agrees with the seasonal variation in POC export of 4.3 - 9.7 $\text{mmol C m}^{-2} \text{d}^{-1}$ in the SCS (Cai et al., 2015) and of $\sim 4.5 \text{ mmol C m}^{-2} \text{d}^{-1}$ in the NCP at Sta. SEATS in summer reported by Chou et al. (2006).

4.2. Exchange of DIC and its nutrient stoichiometry, and their impact on air-sea CO_2 fluxes

It has been previously established that the SCS basin is a typical OcéMar (Dai et al., 2013), and that the magnitude of its role as a CO_2 source and/or sink depends on the relative contributions of DIC and the nutrient supply to the upper layer as well as the biogeochemical alterations occurring therein. Here, the excess DIC flux ($X_{DIC-DIP}$) is defined as the DIC fluxes subtracted by nutrient fluxes using the Redfield ratio,

$$X_{DIC-DIP} = \int_0^S (F_{DIC})ds - \int_0^S (F_{DIP})ds \times r_{C:P} \quad (4)$$

where, F_{DIC} and F_{DIP} are the DIC and DIP flux, respectively, $r_{C:P}$ is the C to P Redfield ratio (106, Redfield et al., 1963), and $X_{DIC-DIP}$ represents the DIC fluxes after biological removal, which potentially affects the air-sea CO_2 fluxes. For the SCS basin, there are two main $X_{DIC-DIP}$ sources in the upper layer. One is the horizontal transport from the WPS via the Luzon Strait, and the other is the vertical transport from deeper layers via upwelling. To compare them, the horizontal transport of $X_{DIC-DIP}$ ($HX_{DIC-DIP}$) at the Luzon Strait is integrated from the surface to a given study depth, and the vertical transport of $X_{DIC-DIP}$ ($VX_{DIC-DIP}$) is integrated across the entire basin at this depth. These comparisons can identify which processes dominate $X_{DIC-DIP}$ to the upper layer.

The $HX_{DIC-DIP}$ at the Luzon Strait increases from $\sim 0.0 \times 10^6 \text{ mol s}^{-1}$ at the surface to a maximum of $12 \times 10^6 \text{ mol s}^{-1}$ at 650 m (Fig. 15). At depths > 650 m, it decreases slightly and then increases to $11 \times 10^6 \text{ mol s}^{-1}$ at > 2500 m. In contrast, the $VX_{DIC-DIP}$ increases from $\sim 0.0 \times 10^6 \text{ mol s}^{-1}$ at the surface to a maximum of $5.9 \times 10^6 \text{ mol s}^{-1}$

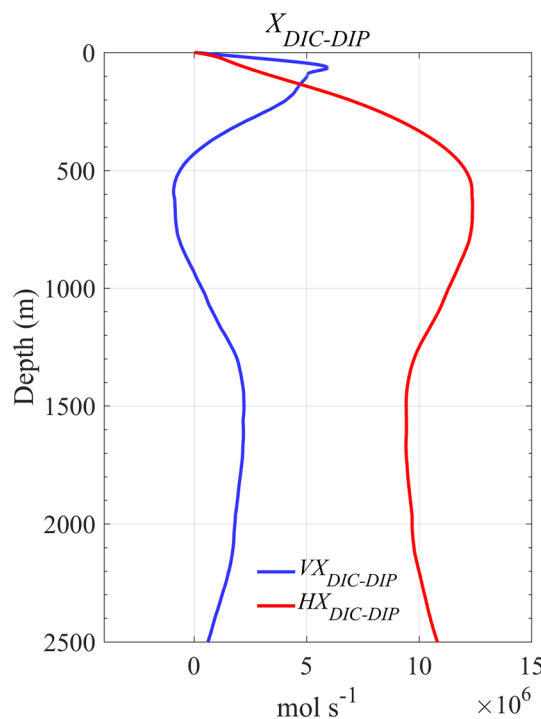


Fig. 15. Depth profiles of vertical excess dissolved inorganic carbon (DIC) fluxes integrated over the South China Sea basin ($VX_{DIC-DIP}$) and horizontal excess DIC fluxes integrated from the surface to a study depth at the Luzon Strait ($HX_{DIC-DIP}$).

at ~ 70 m, and then decreases rapidly to attain a minimum of $-0.9 \times 10^6 \text{ mol s}^{-1}$ at 600 m (Fig. 15). At $h > 600$ m, it again increases to a maximum of $2.2 \times 10^6 \text{ mol s}^{-1}$ at 1600 m, and then decreases to $\sim 0.0 \times 10^6 \text{ mol s}^{-1}$ at > 2700 m. In the upper 150 m, $VX_{DIC-DIP}$ is greater than $HX_{DIC-DIP}$, suggesting that the former is the dominant $X_{DIC-DIP}$ source. At 150 - 500 m, $VX_{DIC-DIP}$ decreases rapidly to $\sim 0.0 \times 10^6 \text{ mol s}^{-1}$ at 430 m, while $HX_{DIC-DIP}$ shows a rapid increase with increasing depth, indicating that $VX_{DIC-DIP}$ in the upper 150 m is initially transported from $HX_{DIC-DIP}$ at 150 - 430 m via the Luzon Strait. Thus, if the upper 430 m are considered as a whole, $X_{DIC-DIP}$ is primarily supplied from the $HX_{DIC-DIP}$ via the Luzon Strait, and the $VX_{DIC-DIP}$ at > 430 m exerts little direct influence on the air-sea CO_2 fluxes at the surface at short time scales.

5. Summary

In this study, a well validated, three-dimensional, coupled physical-biogeochemical model is applied to elucidate DIC dynamics in the SCS. The model is able to capture the characteristic differences and the seasonality of θ , salinity, DIC, TALK, NO_3^- and DIP between the basin and shelves, and between the SCS and the WPS.

Influenced by freshwater inputs from riverine runoff, DIC concentrations in surface waters are generally lower in the coastal and plume areas of the Pearl and Mekong Rivers, on the northern shelf in summer and in the Gulf of Thailand throughout the year. The basin

shows higher DIC concentrations in winter and spring than in summer and fall. At 100 m, DIC concentrations in the northeast SCS are lower than in the central basin throughout the year, an effect primarily attributed to the dilution effect of DIC by the Kuroshio intrusion. Concentrations of DIC in the central basin are mostly higher than those in the vicinity of the slope areas, a feature that is more pronounced in winter, and is attributed to upwelling motion in the central basin. In the latter, the spatial and seasonal variation of DIC are also clearly influenced by meso-scale features. Below 200 m and up to 2500 m, a characteristic enhancement of DIC from the WPS to the vicinity of the SCS by up to $140 \mu\text{mol kg}^{-1}$ is observed. This increasing pattern of DIC continues from the northern to the southern basin although to a lesser degree (increase $< 20 \mu\text{mol kg}^{-1}$), in the upper 1400 m.

Spatiotemporal variation of the DIC is controlled by both physical transport and biogeochemical processes in the SCS. Influxes of DIC to the SCS in the upper 600 m and > 1600 m via the Luzon Strait are $12.7 \times 10^6 \text{ mol s}^{-1}$ and $1.8 \times 10^6 \text{ mol s}^{-1}$, respectively, while the DIC outflow occurring in the intermediate layer ($600 \text{ m} < h < 1600 \text{ m}$) via the Luzon Strait is $3.3 \times 10^6 \text{ mol s}^{-1}$. The DIC outflow is $6.8 \times 10^6 \text{ mol s}^{-1}$ at the Mindoro and Balabac Strait, $2.2 \times 10^6 \text{ mol s}^{-1}$ at the Taiwan Strait, and $2.4 \times 10^6 \text{ mol s}^{-1}$ at the Karimata Strait. There is a net transport of DIC from the basin toward the shelves, accounting for $4.8 \times 10^6 \text{ mol s}^{-1}$. Along the 100 m isobath, shelfward DIC transport primarily occurs on the northern and southwestern shelves.

The upward transport of DIC occurs mainly in the upper 400 m and at > 1100 m, which provides the DIC sources for DIC outflow to the WPS in the intermediate layer via the Luzon Strait. The downward water transport in intermediate layers (400 m to 1100 m) creates a barrier for upward DIC transport from the deep to the upper layer. Thus, DIC dynamics in the upper layer are primarily influenced by horizontal DIC transport from Kuroshio intrusion rather than by vertical transport from the deep layer at short time scales.

In the euphotic zone, the DIC budget reveals that HADV and VADV are the dominant terms, but with opposite signs, so they tend to neutralize each other. They can be orders of magnitude greater than the other terms, thus playing important roles in the DIC budget in the SCS basin. Both their absolute values in winter exceed those in summer. The enhanced Kuroshio intrusion and favorable vertical upwelling in winter contribute to this seasonal variation. The decreases in DIC inventory in spring and summer in the euphotic zone are caused by net DIC consumption, while the increases in DIC inventory in fall and winter are primarily influenced by DIC vertical transport. On an annual basis, physical transport and biotic processes are equally important in influencing the seasonal variation in DIC inventories in the upper SCS basin. In the middle and deep layers, only the physical transport term plays an important role in controlling the seasonal variation of DIC inventories.

Fluxes of DIC and their stoichiometry in relation to nutrient fluxes suggest that $VX_{\text{DIC-DIP}}$ is the primary $X_{\text{DIC-DIP}}$ source in the upper 150 m at short timescale that potentially influences air-sea CO_2 fluxes in the SCS. This part of $VX_{\text{DIC-DIP}}$ is initially transported from $HX_{\text{DIC-DIP}}$ at 150 to 430 m via the Luzon Strait. The $VX_{\text{DIC-DIP}}$ from depths > 430 m exerts little immediate influence on the air-sea CO_2 fluxes. Overall, DIC dynamics in the SCS is influenced by a combination of intrinsic and extrinsic forcings, the latter primarily from the WPS, both of which play important roles on DIC distributions, transport, and biogeochemical changes.

It is noteworthy that the model described in this study has not considered the transformation between DIC and dissolved organic carbon (DOC) and CaCO_3 dissolution. Compared to the WPS, the SCS has an excess of $3.2 \pm 1.1 \mu\text{mol DOC kg}^{-1}$ at 1000–1500 m (Dai et al., 2009). Therefore ignoring DOC processes could potentially overestimate DIC concentrations by $\sim 0.13\%$. Additionally, DIC addition from CaCO_3 dissolution is estimated to equal $13 \pm 5 \mu\text{mol kg}^{-1}$ at 200 to 800 m (Cao et al., 2011a), and ignoring this process could potentially underestimate by $\sim 0.6\%$ the DIC concentration in these layers.

Declaration of Competing Interest

The authors declare that they have no known competing financial interests or personal relationships that could have appeared to influence the work reported in this paper.

Acknowledgements

This study was funded by National Natural Science Foundation of China through grants No. 41890801 and 41730533, theme-based Research Scheme (T21-602/16-R) of the Hong Kong Research Grants Council through grant No. GRF16308319, National Basic Research Program of China (973 Program) through grant No. 2015CB954001, China Postdoctoral Science Foundation, and the Outstanding Postdoctoral Scholarship, State Key Laboratory of Marine Environmental Science at Xiamen University, China. The authors thank Zhiqiang Liu for his help with data analysis, Lifang Wang, Tao Huang, Liguang Guo, Yi Xu and Xianghui Guo for their assistance in sampling and/or analysis during the cruises, Yanping Xu for providing observational data, and Zhongya Cai for his useful suggestions. Discussions with Weijun Cai from University of Delaware and Eileen E. Hofmann from Old Dominion University were also very helpful.

Appendix A. Supplementary material

Supplementary data to this article can be found online at <https://doi.org/10.1016/j.pcean.2020.102367>.

References

- Borges, A.V., Delille, B., Frankignoulle, M., 2005. Budgeting sinks and sources of CO_2 in the coastal ocean: diversity of ecosystems counts. *Geophys. Res. Lett.* 32, L14601.
- Cai, P., Zhao, D., Wang, L., Huang, B., Dai, M., 2015. Role of particle stock and phytoplankton community structure in regulating particulate organic carbon export in a large marginal sea. *J. Geophys. Res. Oceans* 120, 2063–2095. <https://doi.org/10.1002/2014JC010432>.
- Cai, W.-J., 2011. Estuarine and coastal ocean carbon paradox: CO_2 sinks or sites of terrestrial carbon incineration? *Annu. Rev. Mar. Sci.* 3, 123–145.
- Cai, W.-J., Dai, M., Wang, Y., 2006. Air-sea exchange of carbon dioxide in ocean margins: A province-based synthesis. *Geophys. Res. Lett.* 33, L12603. <https://doi.org/10.1029/2006GL026219>.
- Cao, Z., Dai, M., 2011. Shallow-depth CaCO_3 dissolution: Evidence from excess calcium in the South China Sea and its export to the Pacific Ocean. *Global Biogeochem. Cy.* 25, GB2019. <https://doi.org/10.1029/2009GB003690>.
- Cao, Z., Dai, M., Zheng, N., Wang, D., Li, Q., Meng, F., Gan, J., 2011. Dynamics of the carbonate system in a large continental shelf system under the influence of both a river plume and coastal upwelling. *J. Geophys. Res.-Biogeo.* 116, G02010. <https://doi.org/10.1029/2010JG001596>.
- Cao, Z., Yang, W., Zhao, Y., Guo, X., Yin, Z., Du, C., Zhao, H., Dai, M., 2020. Diagnosis of CO_2 dynamics and fluxes in global coastal oceans. *Natl. Sci. Rev.* 7, 786–797. <https://doi.org/10.1093/nsr/nwz105>.
- Chai, F., Liu, G., Xue, H., Shi, L., Chao, Y., Tseng, C.M., Chou, W.C., Liu, K.K., 2009. Seasonal and interannual variability of carbon cycle in South China Sea: a three-dimensional physical-biogeochemical modeling study. *J. Oceanogr.* 65 (5), 703–720.
- Chen, C.T.A., Wang, S.L., Wang, B.J., Pai, S.C., 2001. Nutrient budgets for the South China Sea basin. *Mar. Chem.* 75, 281–300.
- Chen, C.T.A., Wang, S.L., Chou, W.C., Sheu, D.D., 2006. Carbonate chemistry and projected future changes in pH and CaCO_3 saturation state of the South China Sea. *Mar. Chem.* 101, 277–305.
- Chen, C.-T.A., Borges, A.V., 2009. Reconciling opposing views on carbon cycling in the coastal ocean: Continental shelves as sinks and near-shore ecosystems as sources of atmospheric CO_2 . *Deep-Sea Res. II* 56, 578–590.
- Chen, Y.L.L., Chen, H.-Y., 2006. Seasonal dynamics of primary and new production in the northern South China Sea: The significance of river discharge and nutrient advection. *Deep-Sea Res. I* 53, 971–986.
- Chen, Y.L.L., 2005. Spatial and seasonal variations of nitrate-based new production and primary production in the South China Sea. *Deep-Sea Res. I* 52, 319–340. <https://doi.org/10.1016/j.dsr.2004.11.001>.
- Chou, W.C., Sheu, D.D., Chen, C.T.A., Wang, S.L., Tseng, C.M., 2005. Seasonal variability of carbon chemistry at the SEATS time-series site, northern South China Sea between 2002 and 2003. *Terr. Atmos. Ocean. Sci.* 16, 445–465.
- Chou, W.C., Chen, Y.-L.L., Sheu, D.D., Shih, Y.-Y., Han, C.-A., Cho, C.L., Tseng, C.-M., Yang, Y.-J., 2006. Estimated net community production during the summertime at the SEATS time-series study site, northern South China Sea: Implications for nitrogen fixation. *Geophys. Res. Lett.* 33, L22610. <https://doi.org/10.1029/2005GL025365>.
- Chou, W.C., Sheu, D.D., Lee, B.S., Tseng, C.M., Chen, C.T.A., Wang, S.L., Wong, G.T.F.,

- 2007a. Depth distribution of alkalinity, TCO₂ and δ¹³C_{TCO2} at SEATS time-series site, northern South China Sea: Controlling processes and anthropogenic CO₂ influence. *Deep Sea Res., II* 54, 1469–1485. <https://doi.org/10.1016/j.dsr2.2007.05.002>.
- Chou, W.C., Sheu, D.D., Chen, C.T.A., Wen, L.-S., Yang, Y., Wei, C.-L., 2007b. Transport of the South China Sea subsurface water outflow and its influence on carbon chemistry of Kuroshio waters off southeastern Taiwan. *J. Geophys. Res.* 112, C12008. <https://doi.org/10.1029/2007JC004087>.
- Chou, W.C., Gong, G.C., Tseng, C.M., Sheu, D.D., Hung, C.C., Chang, L.P., Wang, L.M., 2011. The carbonate system in the East China Sea in winter. *Mar. Chem.* 123, 44–55.
- Dai, M., Meng, F., Tang, T., Kao, S.-J., Lin, J., Chen, J., Huang, J., Tian, J., Gan, J., Yang, S., 2009. Excess total organic carbon in the intermediate water of the South China Sea and its export to the North Pacific. *Geochem. Geophys. Geosyst.* 10, Q12002. <https://doi.org/10.1029/2009GC002752>.
- Dai, M., Cao, Z., Guo, X., Zhai, W., Liu, Z., Yin, Z., Xu, Y., Gan, J., Hu, J., Du, C., 2013. Why are some marginal seas sources of atmospheric CO₂? *Geophys. Res. Lett.* 40, 2154–2158.
- Du, C., Liu, Z., Dai, M., Kao, S.-J., Cao, Z., Zhang, Y., Huang, T., Wang, L., Li, Y., 2013. Impact of the Kuroshio intrusion on the nutrient inventory in the upper northern South China Sea: insights from an isopycnal mixing model. *Biogeosciences* 10, 1–14.
- Du, C., Liu, Z., Kao, S.-J., Dai, M., 2017. Diapycnal fluxes of nutrients in an oligotrophic oceanic regime: The South China Sea. *Geophys. Res. Lett.* 44. <https://doi.org/10.1002/2017GL074921>.
- Fang, G., Wang, Y., Wei, Z., Fang, Y., Qiao, F., Hu, X., 2009. Inter-ocean circulation and heat and freshwater budgets of the South China Sea based on a numerical model. *Dynam. Atmos. Oceans* 47, 55–72.
- Fennel, K., Wilkin, J., Levin, J., Moisan, J., O'Reilly, J., Haidvogel, D., 2006. Nitrogen cycling in the Middle Atlantic Bight: results from a three-dimensional model and implications for the North Atlantic nitrogen budget. *Global Biogeochem. Cy.* 20 (3) GB3007, doi:3010.1029/2005GB002456.
- Gan, J., Qu, T., 2008. Coastal jet separation and associated flow variability in the southwest South China Sea. *Deep-Sea Res. I* 55, 1–19. <https://doi.org/10.1016/j.dsr.2007.09.008>.
- Gan, J., Liu, Z., Hui, C., 2016a. A three-layer alternating spinning circulation in the South China Sea. *J. Phys. Oceanogr.* 46, 2309–2315. <https://doi.org/10.1175/JPO-D-16-0044>.
- Gan, J., Liu, Z., Liang, L., 2016b. Numerical modeling of intrinsically and extrinsically forced seasonal circulation in the China Seas: A kinematic study. *J. Geophys. Res. Oceans* 121. <https://doi.org/10.1002/2016JC011800>.
- Gan, J., Lu, Z., Cheung, A., Dai, M., Liang, L., Harrison, P., Zhao, X., 2014. Assessing ecosystem response to phosphorus and nitrogen limitation in the Pearl River plume using the Regional Ocean Modeling System (ROMS). *J. Geophys. Res. Oceans* 119, 8858–8877. <https://doi.org/10.1002/2014JC009951>.
- Gan, J., Lu, Z., Dai, M., Cheung, A., Harrison, P., Liu, H., 2010. Biological response to intensified upwelling and to a river plume in the northeastern South China Sea: A modeling study. *J. Geophys. Res.* 115, C09001. <https://doi.org/10.1029/2009JC005569>.
- Gong, G.C., Liu, K.-K., Liu, C.T., Pai, S.C., 1992. The chemical hydrography of the South China Sea west of Luzon and a comparison with the West Philippine Sea. *Terr. Atmos. Ocean Sci.* 3, 587–602.
- Guo, X.H., Zhai, W.D., Dai, M.H., Zhang, C., Bai, Y., Xu, Y., Li, Q., Wang, G.Z., 2015. Air-sea CO₂ fluxes in the East China Sea based on multiple-year underway observations. *Biogeosciences* 12, 5495–5514.
- Hofmann, E.E., Cahill, B., Fennel, F., Friedrichs, M.A., Hyde, K., Lee, C., Mannino, A., Najjar, R.G., O'Reilly, J.E., Wilkin, J., 2011. Modeling the dynamics of continental shelf carbon. *Annu. Rev. Mar. Sci.* 3, 93–122.
- Laruelle, G.G., Cai, W.-J., Hu, X., Gruber, N., Mackenzie, F.T., Regnier, P., 2018. Continental shelves as a variable but increasing global sink for atmospheric carbon dioxide. *Nat. Commun.* 9 (454). <https://doi.org/10.1038/s41467-017-02738-z>.
- Li, L., Qu, T., 2006. Thermohaline circulation in the deep South China Sea basin inferred from oxygen distributions. *J. Geophys. Res.* 111, C05017. <https://doi.org/10.1029/2005JC003164>.
- Li, Q., Guo, X., Zhai, W., Xu, Y., Dai, M., 2020. Partial pressure of CO₂ and air-sea CO₂ fluxes in the South China Sea: Synthesis of an 18-year dataset. *Prog. Oceanogr.* 182 (102272). <https://doi.org/10.1016/j.pocean.2020.102272>.
- Liu, Z., Gan, J., 2016. Open boundary conditions for tidally and subtidally forced circulation in a limited-area coastal model using the Regional Ocean Modeling System (ROMS). *J. Geophys. Res. Oceans* 121 (8), 6184–6203. <https://doi.org/10.1002/2016JC011975>.
- Liu, Z., Gan, J., 2017. Three-dimensional pathways of water masses in the South China Sea: A modeling study. *J. Geophys. Res. Oceans* 122, 6039–6054. <https://doi.org/10.1002/2016JC012511>.
- Lu, Z., Gan, J., Dai, M., 2012. Modeling seasonal and diurnal pCO₂ variations in the northern South China Sea. *J. Mar. Syst.* 92 (1), 30–41. <https://doi.org/10.1016/j.jmarsys.2011.10.003>.
- Lu, Z., Gan, J., Dai, M., Zhao, X., Hui, C.R., 2020. Nutrient transport and dynamics in the South China Sea: A modeling study. *Prog. Oceanogr.* 183, 102308.
- Qu, T., Mitsudera, H., Yamagata, T., 2000. Intrusion of the North Pacific waters into the South China Sea. *J. Geophys. Res.* 105, 6415–6424.
- Redfield, A.C., Ketchum, B.H., Richards, F.A., 1963. The influence of organisms on the composition of seawater. In: Hill, M.N. (Ed.), *The Sea*. Wiley, New York, pp. 26–77.
- Roberts, E., Dai, M., Cao, Z., Zhai, W., Guo, L., Sameul, S.P., Du, C., 2020. The carbonate system of the northern South China Sea: seasonality and exchange with the western North Pacific. *Prog. Oceanogr.* (submitted for publication).
- Sheu, D.D., Chou, W.-C., Chen, C.T.A., Wei, C.L., Hsieh, H.L., Hou, W.P., Dai, M.H., 2009. Riding over the Kuroshio from the South to the East China Sea: Mixing and transport of DIC. *Geophys. Res. Lett.* 36, L07603.
- Sheu, D.D., Chou, W.-C., Wei, C.-L., Hou, W.-P., Wong, G.T.F., Hsu, C.-W., 2010. Influence of El Niño on the sea-to-air CO₂ flux at the SEATS time-series site, northern South China Sea. *J. Geophys. Res.* 115, C10021. <https://doi.org/10.1029/2009JC006013>.
- Tan, S.-C., Shi, G.-Y., 2009. Spatiotemporal variability of satellite-derived primary production in the South China Sea, 1998–2006. *J. Geophys. Res.* 114, G03015. <https://doi.org/10.1029/2008JG000854>.
- Tian, J.W., Yang, Q.X., Liang, X.F., Xie, L.L., Hu, D.X., Wang, F., Qu, T.D., 2006. Observation of Luzon Strait transport. *Geophys. Res. Lett.* 33 (L19607).
- Tian, J.W., Wang, Q.X., Zhao, W., 2009. Enhanced diapycnal mixing in the South China Sea. *J. Phys. Oceanogr.* 39, 3191–3203.
- Tseng, C.-M., Wong, G.T.F., Chou, W.-C., Lee, B.-S., Sheu, D.-D., Liu, K.-K., 2007. Temporal variations in the carbonate system in the upper layer at the SEATS station. *Deep-Sea Res. II* 54, 1448–1468.
- Wanninkhof, R., 1992. Relationship between wind-speed and gas-exchange over the ocean. *J. Geophys. Res. Oceans* 97 (C5), 7373–7382.
- Weiss, R.F., 1974. Carbon dioxide in water and seawater: the solubility of a non-ideal gas. *Mar. Chem.* 2, 203–215.
- Yang, Q.X., Tian, J.W., Zhao, W., 2011. Observation of material fluxes through the Luzon Strait. *Chin. J. Oceanol. Limn.* 29 (1), 26–32.
- Zhai, W., Dai, M., Cai, W.-J., Wang, Y., Hong, H., 2005. The partial pressure of carbon dioxide and air-sea fluxes in the northern South China Sea in spring, summer and autumn. *Mar. Chem.* 96 (1–2), 87–97. <https://doi.org/10.1016/j.marchem.2004.12.002>.
- Zhai, W., Dai, M., Chen, B., Guo, X., Li, Q., Shang, S., Zhang, C., Cai, W.-J., Wang, D., 2013. Seasonal variations of air-sea CO₂ fluxes in the largest tropical marginal sea (South China Sea) based on multiple-year underway measurements. *Biogeosciences* 10, 7775–7791.